**University of Alberta**

**Library Release Form**

**Name of Author**: M. Jahrul Alam

**Title of Thesis**: A Fully Lagrangian Advection Scheme for Electro-Osmotic Flow

**Degree**: Master of Science

**Year this Degree Granted:** 2000



---

Department of Mathematical Sciences

University of Alberta

Edmonton, Alberta

Canada. T6G 2G1

October 2, 2000

University of Alberta

# A Fully Lagrangian Advection Scheme for Electro-Osmotic Flow

by

M. Jahrul Alam

A thesis submitted to the Faculty of Graduate Studies and Research
in partial fulfillment of the requirements of the degree of
Master of Science

in

Applied Mathematics

Department of Mathematical Sciences
Edmonton, Alberta
Fall, 2000

**University of Alberta**

**Faculty of Graduate Studies and Research**

The undersigned certify that they have read and recommend to the Faculty of Graduate Studies and Research for acceptance, a thesis entitled **A Fully Lagrangian Advection Scheme for Electro-osmotic Flow,** submitted by **M. Jahrul Alam** in partial fulfillment of the requirements for the degree of **Master of Science** in **Applied Mathematics.**

---

Dr. John C. Bowman, Supervisor

---

Dr. Christopher J. Backhouse

---

Dr. Bruce R. Sutherland

---

Dr. Walter Allegretto

**Abstract**

A numerical model to study passive scalar advection is described. The advecting velocity field is computed by solving the incompressible Navier–Stokes equation. The method uses a semi-implicit multigrid algorithm to compute the divergence-free velocity at each grid point. The finite differences are second-order accurate and centered in space. However, the traditional second-order compact finite differencing of the Poisson equation for the pressure field is shown not to conserve energy in the inviscid limit. We have designed a non-compact finite differencing for the Laplacian in the pressure equation that conserves energy and affords second-order accuracy. A new numerical method for advection is also developed. This method, which we call parcel advection, is applied to study transport due to electro-osmosis and electrophoresis. The numerical experiments show that parcel advection predicts the evolution of a passively traveling scalar pulse to high accuracy without requiring the addition of any artificial diffusion.

**Acknowledgements**

I would like to express my sincere thanks to my supervisor, Dr. John C Bowman. This work would not have been completed without his guidance and enthusiasm. I would also like to thank my wife, Jesmin Sultana, for her continued encouragement. Many other people helped me with encouragement, suggestions and in proof reading. Without producing a long list of them, I am grateful to every one who helped me in different ways to complete the thesis.

# Contents

# List of Figures

# Chapter 1

# INTRODUCTION

## 1.1 Motivation

Many practical problems in science and engineering, especially in the field of fluid dynamics, involve passive advection of scalar quantities. A scalar field is said to be passive if its amplitude is small enough not to affect appreciably the density and the other physical properties of the fluid (Leslie 1973, p.156). One of the most important passive advection problems associated with the application of an electric field to a mixture of charged species in solution is capillary electrophoresis (Culbertson & Jorgenson 1994). Extensive experimental studies of capillary electrophoresis have been performed (Jorgenson & Lukacs 1981) in the field of microfluidics and chemical analysis of biological fluids—for example, protein separation and/or DNA transport. In

laboratory experiments, the solvent flow could be directed along a specified capillary by the application of appropriate voltages (Harrison *et al.* 1992). In most of these experiments, the sample was injected with electro-osmotic flow driven by an applied potential along the channel (Harrison *et al.* 1993; Seiler *et al.* 1994). In the case of a cross-channel device, the shape of the injected sample, which is an important parameter that influences the resolution of the separated zones during the electrophoresis, depends primarily on the electro-osmotic flow pattern at the intersection of the channels. The electro-osmotic flow itself is influenced by various parameters, such as the Reynolds number, applied potential gradient, and electrophoretic mobility. Until now many experimental and theoretical investigations have been performed to determine the parameters that give the most desirable shape of the injected sample. An analytical attempt to investigate electro-osmotic flow in a single long uniform capillary can be found in Rice & Whitehead (1965), Burgreen & Nakache (1964), and Andreev & Lisin (1993). Two-dimensional computer simulations of electrokinetic injection and transport for a cross-channel device are described in Ermakov *et al.* (1998, 2000). A steady-state three-dimensional simulation (Patankar & Hu 1998) was performed to study the electro-osmotic flow in a cross-channel microfluidic device. However, relatively little attention has been paid to the advection of a charged species either in numerical simulations or in theoretical studies.

Over the last few decades, there has been an increasing interest in the field of computational fluid dynamics. A number of numerical algorithms have been devised

for the simulation of many practical problems in science and engineering that involve passive advection of scalar quantities and lead to partial differential equations of the hyperbolic type. Scalar transport phenomenon naturally arise in a wide variety of applications. One particular example that we will be dealing with throughout this study is the separation of chemical species by capillary electrophoresis. A major difficulty which has enlivened research in this area is the problem of simulating advection. The special difficulty associated with these simulations is the formation of shock and contact discontinuities. With minor modifications, the first solution for representing shock and contact discontinuities was proposed by Neumann & Richtmyer (1950). However, certain disadvantages of von Neumann and Richtmyer's approach have led to continued efforts in developing more convenient, more accurate, and/or more elegant solutions. An elementary approach in modeling advection on a computer is the finite difference method. In the area of computational fluid dynamics there have been two basic approaches to applying the finite difference method to the governing partial differential equations. One is the Eulerian approach and the other is the Lagrangian approach. The Eulerian approach deals with a system of coordinates that is fixed in space. On the other hand the Lagrangian approach deals with a system of coordinates which follows the fluid as it moves. The first hydrodynamic initial value problems that were tried on a computer were one dimensional in space (Schulz 1964). In one dimension the arguments in favour of a Lagrangian over an Eulerian formulation are almost overwhelming. Eulerian codes in general are not as accurate

and have additional troubles. If the system is compressed, definition is lost due to the fixed-in-space nature of the coordinates in Eulerian codes, in contrast to the fixed-in-the-material nature of the coordinates in Lagrangian codes. One of the most severe drawbacks of the Eulerian method is the difficulty found in dealing correctly with the advective term $\boldsymbol{v} \cdot \boldsymbol{\nabla} \boldsymbol{v}$. In the case of scalar advection, if the scalar quantity is the concentration of the tracer field, this quantity must always be non-negative. Without proper handling of the advective term, the numerical solution can go unconditionally unstable, producing negative concentration or spurious wiggles (Tannehill *et al.* 1997). There are a wide variety of finite-difference approaches that can be used to represent the advective derivative on a numerical grid. Unfortunately all of them must respect a Courant–Friedrich–Lewy criterion to remain stable, (e.g. see Press *et al.* (1997)). In addition, they not only suffer from dispersive and diffusive error but also destroy the conservative properties of the equation (Press *et al.* 1997). Historically, the first alternative was the unconditionally stable method of characteristics introduced by Courant *et al.* (1952) sometimes referred to as the CIR scheme (LeVeque 1990). Since this method uses interpolation based on the nearest grid point, in spite of the unconditional stability of the method, its overall performance is affected by the inherent computational damping associated with the interpolation (Ritchie 1986). To address this problem, Ritchie (1986) proposed to decompose the displacement vector into the sum of two vectors, one of which goes to the nearest grid point. The other vector, the residual, is treated with an Eulerian method. However, the

method of Ritchie still introduces dispersion of the Eulerian component (Staniforth & Cote 1991). Another attractive way of handling the solution of advection-dominated flow problems in complex geometries is the finite element method. However at high Reynolds numbers, standard Galerkin-based finite element methods are not suitable and must be stabilized (Minev & Ethier 1999).

The aim of this study is to develop a fully Lagrangian algorithm for simulating passive scalar advection by electro-osmotic flow.

## 1.2 Physical background

The phenomena that we will be dealing with throughout this study are the effects associated with the movement of ionic solution near a charged interface (Morrison & Stukel 1970). It plays an important role in many diverse natural and technological processes such as in the biotechnology industry, biochemical, and biological research. Electrophoresis has sufficient resolving power to distinguish between long-chain polynucleotides. Sample sizes for electrophoresis are in the nanoliter range. The bulk behavior of a solution of charged particles is a complicating feature. This becomes more complicated because of the dynamics of the diffuse space charge that arises from the response of the ions to the charged interface (Levine & Neale 1976). However, if this complication is ignored, the dynamics of a small charged particle in

an ionic solution can be understood from the description of the electric fields and forces in the fluid and on the particle (Ermakov *et al.* 2000).

Let us consider an electrophoresis system consisting of a channel with a rectangular cross section filled with a buffering medium across which a voltage is applied. A schematic diagram of the electric double layer that develops at the charged interface and the diffuse outer layer of the double layer is shown in Fig. 1.1. Suppose that the wall of the channel is negatively charged and a positive voltage is applied at the input reservoir on the left end of the channel. Because of the applied voltage, positive charges will move toward the negative electrode (Reed & Morrison 1976). The overall dynamics is associated with two types of phenomena: electrophoresis and electro-osmosis.

## 1.3 Electrophoresis

Electrophoresis refers to the migration of charged electrical species that are dissolved or suspended in an electrolyte through which an electric current is passed (Moyer & Gorin 1990). Cations migrate toward the negatively charged electrode (cathode) and anions are attracted toward the positively charged electrode (anode). Neutral solutes are not attracted to either electrode. Conventionally, electrophoresis has been performed in layers of gel or paper (Bier 1959). The advantages of conducting electrophoresis in capillaries was highlighted by Jorgenson & Lukacs (1981).

## 1.4 Electro-osmosis

Electro-osmotic flow in micro-channels is critical to the design and process control of various on-chip microfluidic devices such as modern instruments used in chemical analysis and biomedical diagnostics. Generally, all the solid–liquid interfaces have electrical charge. These electrical charges will attract the counter-ions in the electrically neutral liquid; hence there is a layer of liquid near the solid surface where the counter-ion concentration is higher than the co-ion concentration (Arulanandam & Li 2000). In other words, there is a layer near the charged interface that has a net electrical charge concentrated in a small volume. When an electrical field is applied to the liquid, the excess counter-ions in the Debye layer will move under the applied electrical field. These ions will migrate to the electrode that has opposite sign. The moving ions will interact frictionally with the surrounding fluid, pulling it with them and generating a motion of the bulk liquid. This is the so-called electro-osmotic flow. The rate of electro-osmotic flow is generally greater than the electrophoretic migration velocity of the individual species. The total velocity of a species is the vector sum of the electro-osmotic velocity and electrophoretic velocity. Even though the species move according to their charge within the capillary, the electro-osmotic flow rate is sometimes sufficient to sweep all the positive, negative and neutral species in one direction (Skoog *et al.* 1998). This is illustrated in Fig. 1.3.

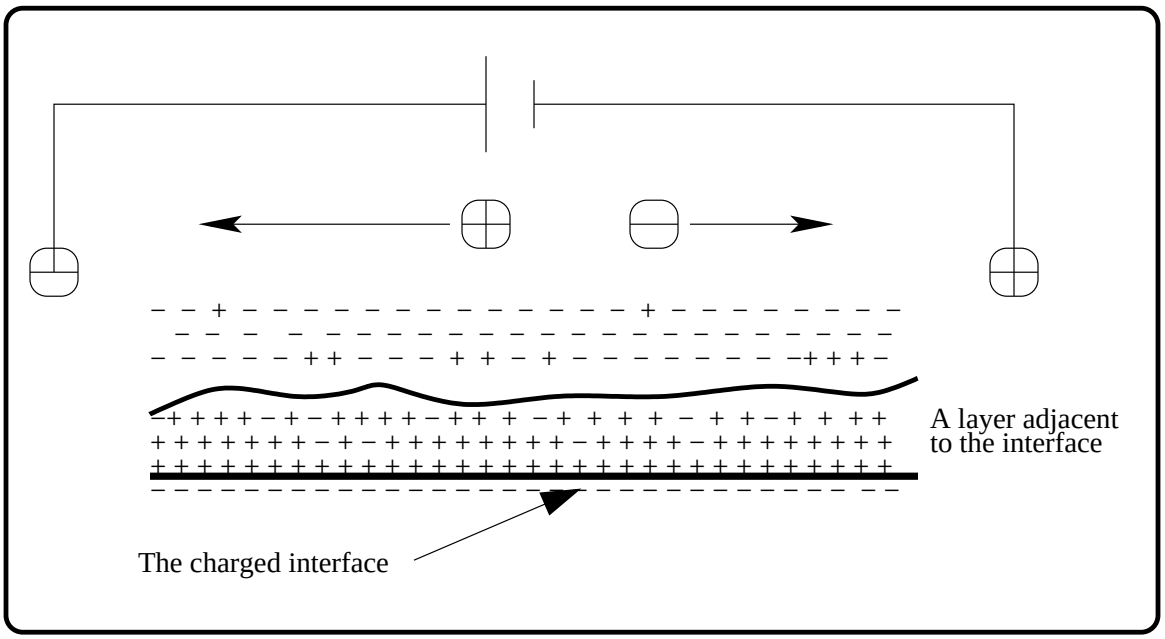


Figure 1.1: A schematic diagram of the Debye layer.

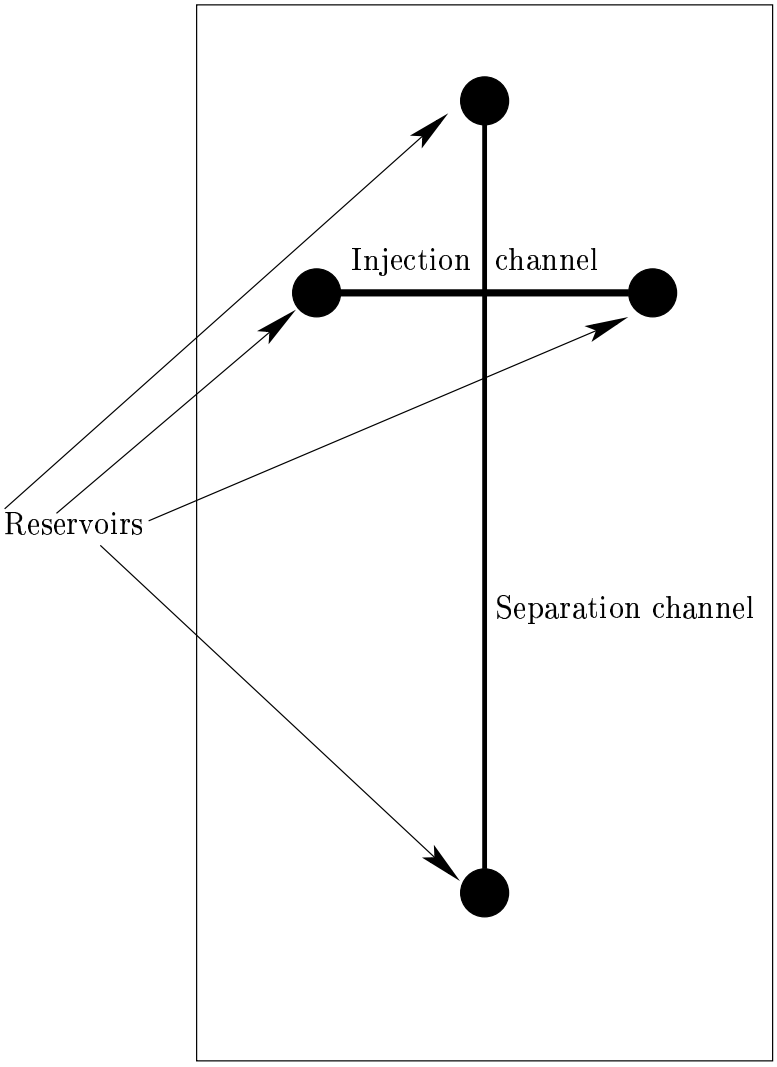


Figure 1.2: A schematic diagram of a microfluidic chip.

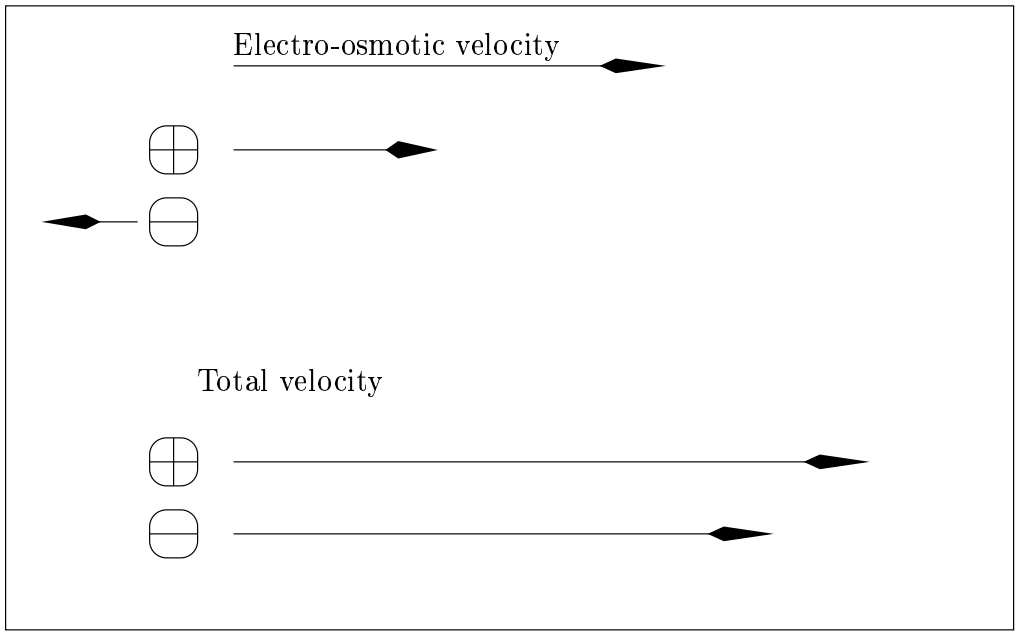


Figure 1.3: Total velocity of ions in response to electric field.

# Chapter 2

# MODEL DEVELOPMENT

## 2.1 Charge balance equation

In order to understand the dynamics near a charged interface, a description of the forces that act in the fluid and particles is essential. The fundamental equations of motion for electro-osmotic flow and passive scalar advection will be described in Section 2.2. First, it is necessary to have an understanding of the electrical force and charge balance equations. One may explain the effect of an applied potential on a charged species from the following simple mathematical argument (Gaál *et al.* 1980).

Assume that we have a species with net charge $Q$, which is suspended in a fluid that behaves as a perfect insulator. If a uniform time-independent electric field $E$ is applied, a force, $QE$, will act on it. The result is the migration of the particle toward

the electrode that has opposite sign. Once the particle starts to move from rest, a frictional force $fv$ acts in the opposite direction, where $f$ is the frictional coefficient and $v$ is the velocity of the particle relative to the surrounding fluid. If $m$ is the mass of the particle, one can write the following differential equation according to Newton's law of motion,

$$m\frac{dv}{dt} = QE - fv, \tag{2.1}$$

or,

$$\frac{dv}{dt} + \frac{f}{m}v = \frac{QE}{m}. \tag{2.2}$$

The solution of (2.2) is

$$v = \frac{QE}{f} + Ce^{-\frac{f}{m}t}.$$

Since we are dealing with micron or smaller sized particles, for a typical charged particle, the factor $f/m$ in the exponential term is order of $10^{14}$ $s^{-1}$ (Gaál *et al.* 1980). Therefore, for times longer than $10^{-14}$ s, the exponential term is negligibly small. Thus, we can write

$$v \approx \frac{QE}{f}. \tag{2.3}$$

This implies that if the electric field is turned on, the particle accelerates rapidly until the electrical force is balanced by the frictional force. Then it migrates at a constant velocity, which is known as the electrophoretic velocity. In reality, the presence of an ionic shield around the particle results in electrophoretic friction and consequently the electrophoretic velocities are slower than those predicted by (2.3).

An important parameter in electrophoretic separation is the electrophoretic mobility. This parameter is defined as velocity per unit electrical force and is usually denoted by $\mu$. That is,

$$\begin{aligned}\mu &= \frac{v}{E} \\ &= \frac{Q}{f}.\end{aligned}$$

Therefore, if two species differ either in charge or in frictional force, they will be separated from each other by an electric field. The frictional force depends on the size and shape of the species. This suggests that species of different size will move with different speeds.

In order to find an expression for the force exerted on a fluid, we first need to establish equations that will determine the charge density and electric field intensity from the potential field. The electric field intensity $\boldsymbol{E}$ is related to the potential $\Phi$ by

$$\boldsymbol{E} = -\boldsymbol{\nabla}\Phi,$$

From Maxwell's equations, we know that

$$\boldsymbol{\nabla} \cdot \boldsymbol{E} = \frac{\rho_e}{\epsilon},$$

where $\rho_e$ is the space charge density and $\epsilon$ is the permittivity of the medium. This implies that $\Phi$ satisfies a Poisson equation:

$$\nabla^2\Phi = -\frac{\rho_e}{\epsilon}. \tag{2.4}$$

In the case of electro-osmosis, the solid–liquid interface has an electrical charge. In contact with the solution, this charged interface will have a certain potential, known as the $\zeta$ potential. In the absence of an externally applied electric field, positively and negatively charged ions in the electrolyte solution give rise to this potential. Hence the total potential $\Phi$ will have a contribution due to the charge at the walls and another contribution from the externally applied electric field. It is thus convenient to decompose $\Phi$ as

$$\Phi = \varphi + \psi,$$

where $\varphi$ is the potential due to the externally applied electric field and $\psi$ is the potential due to the space charges inside the domain. Since the applied potential arises only from the charges outside the domain, it satisfies Laplace's equation,

$$\nabla^2 \varphi = 0. \tag{2.5}$$

Using (2.4) and (2.5), it can be shown that the potential $\psi$ can be calculated from the Poisson equation,

$$\nabla^2 \psi = -\frac{\rho_e}{\epsilon}. \tag{2.6}$$

The potential $\psi$ is characterized by the Debye layer thickness $\lambda_D$, which is given by

$$\lambda_D^2 = \frac{kT\epsilon}{e^2 n}, \tag{2.7}$$

where $k$ is the Boltzmann constant, $T$ is the absolute temperature, $e$ is the elementary charge, and $n$ is the concentration of ions.

At a distance from the wall greater than the Debye length $\boldsymbol{\nabla}\psi$ will have a negligible contribution to the electric field intensity. Therefore,

$$\boldsymbol{E} = -\boldsymbol{\nabla}\varphi$$

is a very good approximation. For further simplification, we use the Debye-Hückel approximation (see Appendix A)

$$\nabla^2\psi = \frac{1}{\lambda_D^2}\psi, \tag{2.8}$$

where $\lambda_D$ is defined by (2.7).

The space charge density $\rho_e$ can be expressed in terms of the potential field from (2.6) and (2.8),

$$\rho_e = -\frac{\epsilon}{\lambda_D^2}\psi. \tag{2.9}$$

For a rectangular domain with a Neumann boundary condition in the $y$ direction and Dirichlet boundary condition in the $x$ direction, one can find a solution to (2.8) (see Fig. 2.1), which is given by

$$\psi(y) = -\frac{\cosh\left[(y - h/2)/\lambda_D\right]}{\cosh(\frac{h}{2\lambda_D})}, \tag{2.10}$$

where $h$ is the width of the domain. This solution states that $\psi$ vanishes rapidly as $y \to h/2$ if $\lambda_D$, given by (2.7), is small compared with $h$. Thus there exists a layer near the wall where the potential drop is steep and falls off rapidly far from the wall.

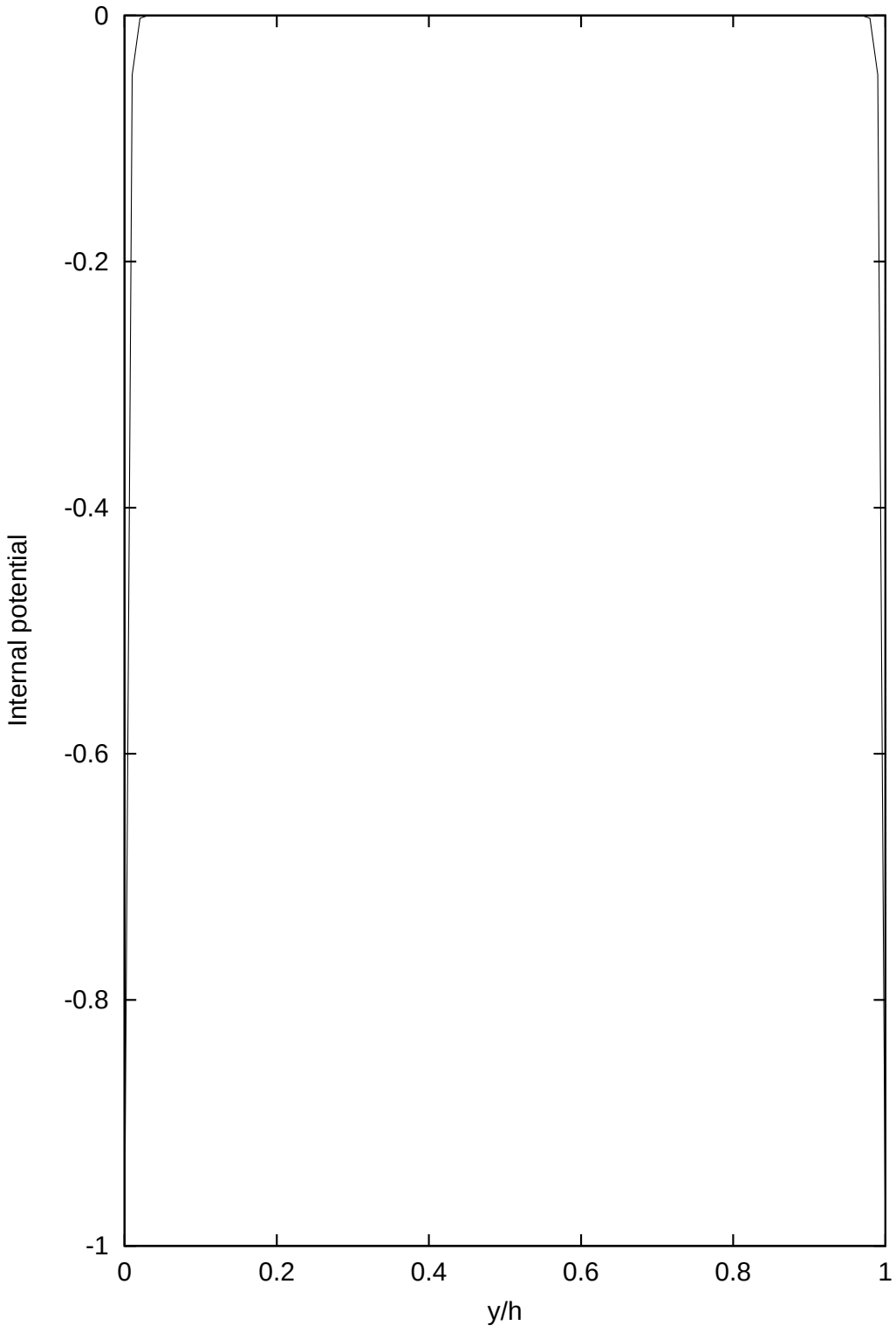


Figure 2.1: Internal potential $\psi$ for $h/\lambda_D = 300$.

## 2.2 The governing equations

The problem of electrophoresis is mathematically similar to the problem of passive scalar advection. The mathematical model that represents the passive advection problem in case of electrophoresis can be formulated using the principles of conservation of *mass, momentum* and *species* (charge). The detailed derivation of the fluid equations can be found in Schlichting (1968) and Kundu (1990) and therefore is not described here. However, we need to make some basic assumptions to come up with a simplified set of equations from the above mentioned conservation laws. We assume that the fluid is incompressible and Newtonian with uniform physical properties and that the concentration of the chemical species dissolved in the fluid is dynamically passive. The complicating structure near the solid liquid interface is ignored since the thickness of the Debye layer is small compared with the characteristic length scale. A fluid is said to be incompressible if the material derivative of the density is zero. When the rate of strain is linearly related to the stress, a fluid is called Newtonian. The dissolved chemical species may lead to a violation of the Newtonian behavior of the fluid (Kundu 1990, p. 93). However, if the concentration is dynamically passive, the Newtonian assumption is a reasonable approximation (Patankar & Hu 1998). Under these assumptions we can write down the following partial differential equations,

Conservation of mass

$$\frac{\partial \rho}{\partial t} + \boldsymbol{\nabla} \cdot (\boldsymbol{v}\rho) = 0, \tag{2.11}$$

Momentum

$$\frac{\partial \boldsymbol{v}}{\partial t} + (\boldsymbol{v} \cdot \boldsymbol{\nabla})\boldsymbol{v} = -\frac{1}{\rho}\boldsymbol{\nabla} P + \nu \nabla^2 \boldsymbol{v} + \boldsymbol{F}, \tag{2.12}$$

Incompressibility

$$\frac{\partial \rho}{\partial t} + \boldsymbol{v} \cdot \boldsymbol{\nabla}\rho = 0, \tag{2.13}$$

Species

$$\frac{\partial C}{\partial t} + \boldsymbol{\nabla} \cdot \boldsymbol{\Gamma} = D\nabla^2 C. \tag{2.14}$$

where $\boldsymbol{v}(\boldsymbol{x}, t)$ is the fluid velocity, $P(\boldsymbol{x}, t)$ is the pressure, $\rho$ is the fluid density (assumed to be constant), $\boldsymbol{F}(\boldsymbol{x}, t)$ is the electrical force per unit mass, $\nu$ is the kinematic viscosity of fluid, and $C(\boldsymbol{x}, t)$ is the concentration of the chemical species dissolved in the fluid. It is assumed that the advected field $C$ is dilute and does not affect the fluid density $\rho$. The concentration flux $\boldsymbol{\Gamma}$ is given by

$$\boldsymbol{\Gamma} = (\boldsymbol{v} + \mu \boldsymbol{E})\, C,$$

where $\mu$ is the electrophoretic mobility (assumed to be constant).

Now (2.11) can be used to reduce (2.13) to the form

$$\boldsymbol{\nabla} \cdot \boldsymbol{v} = 0. \tag{2.15}$$

Thus we have three partial differential equations (2.12, 2.14, 2.15) to solve for three variables $\boldsymbol{v}$, $P$ and $C$. In order to solve these equations we need to know the value of $\boldsymbol{F}$ as well. Note that the concentration appears only in the species conservation equation directly, so that (2.12) and (2.15) are decoupled from (2.14), under the

assumption that the fluid properties are independent of the concentration. Once the velocity field has been computed, we can find the concentration distribution. To compute the advecting velocity, we need to solve the momentum equations coupled with the equations for the pressure and electrical fields.

There are two fundamental approaches to solve (2.12): one is the primitive-variable approach, where the velocity is solved for directly, and the other is the derived-variable approach, where one automatically enforces (2.15) by solving for the velocity vector potential $\boldsymbol{A}$, where $\boldsymbol{v} = \boldsymbol{\nabla} \times \boldsymbol{A}$. Although the second approach has some advantages, its attractiveness is lost when applied to three-dimensional flow (Tannehill *et al.* 1997). Moreover, there are complications in implementing the pressure boundary condition in the vector potential formulation. Although only a two-dimensional code is described in this work, the algorithm has been designed so that it can readily be generalized to a full three-dimensional model. Hence we opt for the former approach, where one solves directly for the velocity variable. Implementation of the incompressibility condition (2.15) then requires special care.

### 2.2.1 Solving for the pressure

The momentum equation is solved for the velocity components using the best available estimate for the pressure distribution. The pressure field is estimated in such a way that a divergence-free velocity field is achieved. An equation for pressure can be

derived by simply taking the divergence of (2.12),

$$\boldsymbol{\nabla} \cdot \left[ \frac{\partial \boldsymbol{v}}{\partial t} + (\boldsymbol{v} \cdot \boldsymbol{\nabla}) \boldsymbol{v} \right] = \boldsymbol{\nabla} \cdot \left[ -\frac{1}{\rho} \boldsymbol{\nabla} P + \nu \nabla^2 \boldsymbol{v} + \boldsymbol{F} \right].$$

Using (2.15) we obtain a Poisson equation, which can be solved for $P$,

$$\nabla^2 P = \rho \boldsymbol{\nabla} \cdot G, \tag{2.16}$$

where

$$\boldsymbol{G} = \boldsymbol{F} - \boldsymbol{v} \cdot \boldsymbol{\nabla} \boldsymbol{v}.$$

An efficient multigrid Poisson solver (Bowman *et al.* 2000) is used to solve this elliptic partial differential equation. The velocity and pressure fields are related in such a way that the pressure field will self-consistently adjust to maintain the solenoidal nature of the velocity field.

### 2.2.2 Determination of the electric force

The force exerted by the applied electric field on a unit volume of fluid containing a space charge density $\rho_e$ is given by

$$\rho \boldsymbol{F} = \rho_e \boldsymbol{E},$$

$$\text{so that} \qquad \boldsymbol{F} = \frac{\epsilon}{\rho \lambda_D^2} \psi \boldsymbol{\nabla} \varphi. \tag{2.17}$$

Upon solving (2.5) and (2.8), we can evaluate the electric force $\boldsymbol{F}$ from (2.17).

### 2.2.3 The model equations

Using a *tilde* to denote *dimensional* quantities, the governing equations can be written, using (2.15) as

$$\frac{\partial \tilde{\boldsymbol{v}}}{\partial \tilde{t}} + \tilde{\boldsymbol{v}} \cdot \tilde{\boldsymbol{\nabla}} \tilde{\boldsymbol{v}} = -\frac{1}{\rho} \tilde{\boldsymbol{\nabla}} \tilde{P} + \tilde{\nu} \tilde{\nabla}^2 \tilde{\boldsymbol{v}} + \frac{\epsilon}{\rho \lambda_D^2} \tilde{\psi} \tilde{\boldsymbol{\nabla}} \tilde{\varphi}, \tag{2.18}$$

$$\frac{\partial \tilde{C}}{\partial \tilde{t}} + \tilde{\boldsymbol{v}} \cdot \tilde{\boldsymbol{\nabla}} \tilde{C} = \tilde{\mu} \tilde{\boldsymbol{\nabla}} \tilde{\varphi} \cdot \tilde{\boldsymbol{\nabla}} \tilde{C} + \tilde{D} \tilde{\nabla}^2 \tilde{C}, \tag{2.19}$$

$$\tilde{\nabla}^2 \tilde{P} = \tilde{\rho} \tilde{\boldsymbol{\nabla}} \cdot \left[ \frac{\epsilon}{\rho \lambda_D^2} \tilde{\psi} \tilde{\boldsymbol{\nabla}} \tilde{\varphi} - \tilde{\boldsymbol{v}} \cdot \tilde{\boldsymbol{\nabla}} \tilde{\boldsymbol{v}} \right], \tag{2.20}$$

$$\tilde{\nabla}^2 \tilde{\psi} = \frac{1}{\lambda_D^2} \tilde{\psi}, \tag{2.21}$$

$$\tilde{\nabla}^2 \tilde{\varphi} = 0. \tag{2.22}$$

## 2.3 Scalings for the variables

The governing equation can now be non-dimensionalized by defining a characteristic length scale and a characteristic velocity scale. An important application of electro-osmotic flow is in nanotechnology and microtechnology, where the typical length scales are $10^{-6}\,\mathrm{m}$ and $10^{-9}\,\mathrm{m}$, respectively. Since the flow characteristics in electro-osmotic pumping are dynamically similar to channel flow, we chose the width $h$ of the capillary tube used in the laboratory experiments as our characteristic length scale. The observed velocity $U$ of a sample in a typical experiment is taken as a characteristic velocity scale.

Accordingly, we introduce the following nondimensional variables, using a *tilde* to to denote the corresponding dimensional variables.

$$\begin{aligned}
\boldsymbol{x} &= \frac{\tilde{x}}{h}, \\
\boldsymbol{v} &= \frac{\tilde{\boldsymbol{v}}}{U}, \\
t &= \frac{U\tilde{t}}{h}, \\
P &= \frac{\tilde{P}}{\rho U^2}, \\
\varphi &= \frac{\tilde{\varphi}}{\Phi_H}, \\
\psi &= \frac{\tilde{\psi}}{\zeta}.
\end{aligned}$$

Here the applied voltage drop $\Phi_H$ at the input reservoir is the characteristic external potential field and the potential due to the charge at the walls is normalized to the wall potential $\zeta$.

### 2.3.1 Dimensionless equation of motion

If we substitute the expressions for the dimensional variables into (2.18)–(2.22), we obtain

$$\frac{U^2}{h}\,\frac{\partial \boldsymbol{v}}{\partial t} + \frac{U^2}{h}\,(\boldsymbol{v}\cdot\boldsymbol{\nabla})\boldsymbol{v} = -\frac{U^2}{h}\,\boldsymbol{\nabla}P + \frac{\tilde{\nu}U}{h^2}\,\nabla^2\boldsymbol{v} + \frac{\zeta\Phi_H}{h}\,\frac{\epsilon}{\rho\lambda_D^2}\psi\boldsymbol{\nabla}\varphi,$$

$$\frac{U}{h}\,\frac{\partial C}{\partial t} + \frac{U}{h}\,(\boldsymbol{v}\cdot\boldsymbol{\nabla})C = \frac{\Phi_H}{h^2}\,(\tilde{\mu}\boldsymbol{\nabla}\varphi\cdot\boldsymbol{\nabla})C + \frac{\tilde{D}}{h^2}\nabla^2 C,$$

$$\frac{U^2}{h^2}\,\nabla^2 P = \frac{1}{h}\,\boldsymbol{\nabla}\cdot\left(\frac{\zeta\Phi_H}{h}\,\frac{\epsilon}{\rho\lambda_D^2}\psi\boldsymbol{\nabla}\varphi - \frac{U^2}{h}\,\boldsymbol{v}\cdot\boldsymbol{\nabla}\boldsymbol{v}\right),$$

$$\frac{\zeta}{h^2}\,\nabla^2\psi = \frac{\zeta}{\lambda_D^2}\psi,$$
$$\frac{\Phi_H}{h^2}\nabla^2\varphi = 0.$$

In dimensionless variables, these equations take the form

$$\frac{\partial \boldsymbol{v}}{\partial t} + \boldsymbol{v}\cdot\boldsymbol{\nabla}\boldsymbol{v} = -\boldsymbol{\nabla}P + \nu_v\nabla^2\boldsymbol{v} + \alpha\psi\boldsymbol{\nabla}\varphi, \tag{2.23}$$

$$\frac{\partial C}{\partial t} + \boldsymbol{v}\cdot\boldsymbol{\nabla}C = \mu\boldsymbol{\nabla}\varphi\cdot\boldsymbol{\nabla}C + \nu_c\nabla^2 C, \tag{2.24}$$

$$\nabla^2 P = \boldsymbol{\nabla}\boldsymbol{\cdot}\left(\alpha\psi\boldsymbol{\nabla}\varphi - \boldsymbol{v}\cdot\boldsymbol{\nabla}\boldsymbol{v}\right), \tag{2.25}$$

$$\nabla^2\psi = \kappa^2\psi, \tag{2.26}$$

$$\nabla^2\varphi = 0, \tag{2.27}$$

where

$$\alpha = \frac{\zeta\Phi_H\epsilon}{\rho U^2\lambda_D^2} = \frac{\zeta\Phi_H e^2 n}{\rho U^2 kT},$$
$$\nu_v = \frac{\nu}{Uh},$$
$$\nu_c = \frac{D}{Uh},$$
$$\mu = \frac{\tilde{\mu}\Phi_H}{Uh},$$
$$\kappa^2 = \frac{h^2}{\lambda_D^2} = \frac{h^2 e^2 n}{kT\epsilon}.$$

Some typical values for different scales can be used to estimate $\nu_v$ and $\nu_c$ (Patankar & Hu 1998; Crabtree *et al.* 2000); *i.e.*,

$$\text{a length scale,}\quad h \sim 5\times 10^{-5}\,\text{m},$$

a velocity scale, $U \sim 10^{-3}$,

diffusion coefficient, $D \sim 10^{-11}\mathrm{m}^2/\mathrm{s}$,

kinemitic viscosity of fluid, $\nu \sim 10^{-6}\mathrm{m}^2/\mathrm{s}$.

Using these typical values, we find that $\nu_v \sim 20$ and $\nu_c \sim 10^{-4}$. Hence the velocity field is dominated by viscosity and the concentration field is dominated by advection.

Equation (2.23)–(2.27) are five equations with five unknowns and they make a closed system. The fact that (2.26) and (2.27) are time independent can be exploited in a numerical implementation of this system of equations.

## 2.4 Geometry and boundary conditions

### 2.4.1 The computational geometry

We are interested in modeling passive advection in a simple geometry throughout this study. Widely used laboratory instruments for capillary electrophoresis are designed with L-shaped, T-shaped or curved channels. More recently, computers have been used in modeling electrophoretic transport and extensive investigations have been performed both theoretically and experimentally. As well, mathematical models have been developed (Allison & Nambi 1994). Early mathematical models were one-dimensional and equations were simplified to one dimension based on arbitrary

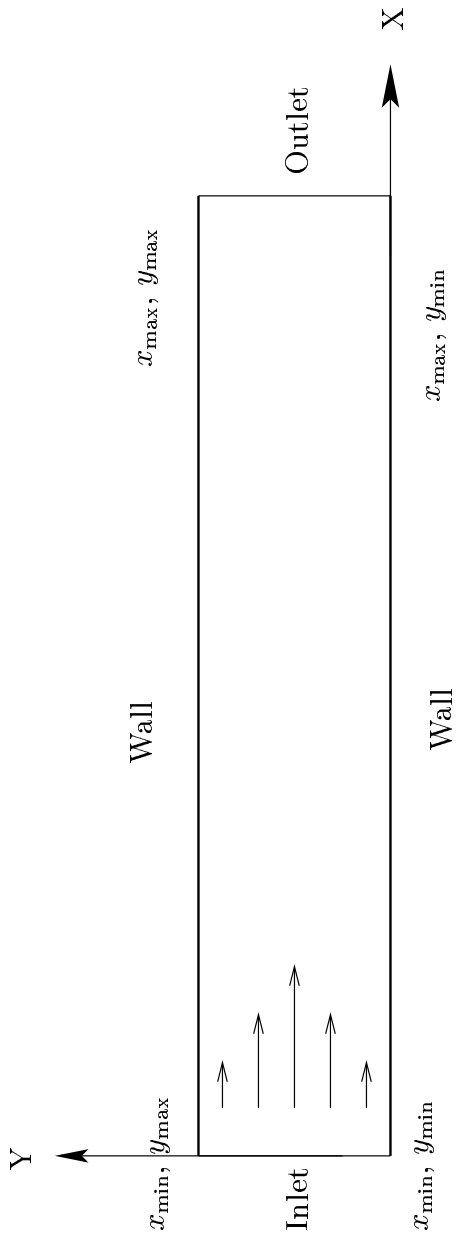


Figure 2.2: The computational geometry (overhead view)

.

initial and boundary conditions (Andreev & Lisin 1993; Bowen *et al.* 1976; Burgreen & Nakache 1964). Recently, a three-dimensional simulation has been performed to analyze steady-state electro-osmotic flow (Patankar & Hu 1998) and has indicated that the vertical component of velocity is small compared with that of the horizontal component. We are mainly interested in simulating passive advection, where the velocity field is specified by an unsteady flow. The advection in the vertical direction by such a velocity field can be neglected. Thus in this work we restrict our attention to a two-dimensional flow. In our simulation, the computational domain is given by

$$\Omega = \{(x, y) : x_{\min} \leq x \leq x_{\max},\ y_{\min} \leq y \leq y_{\max}\},$$

which represents the along-channel cross section of the capillary, as illustrated in Fig. (2.2).

### 2.4.2 Boundary condition on the potential field

Usually an electric field is applied in the along-channel direction by imposing a voltage drop between two of the opposing reservoirs depicted in Fig. 1.2. A Dirichlet boundary condition is used at the input and output reservoir. We use the non-dimensional value $1$ at the input boundary and $0$ at the output boundary for $\varphi$:

$$\varphi(x_{\min}, y) = 1 \quad \text{and} \quad \varphi(x_{\max}, y) = 0.$$

We use a Neumann boundary condition at the walls (Levine & Neale 1976),

$$\frac{\partial \varphi}{\partial y}(x, y_{\min}) = 0 \quad \text{and} \quad \frac{\partial \varphi}{\partial y}(x, y_{\max}) = 0.$$

For the potential due to the charge in the fluid, we use a Dirichlet boundary condition on the walls. To model a solid–liquid interface that has a negative charge, we use the non-dimensional value $-1$ for $\psi$ at the walls. We use a Neumann boundary condition for $\psi$ at the inlet and outlet boundaries:

$$\frac{\partial \psi}{\partial x}(x_{\min}, y) = 0 \quad \text{and} \quad \frac{\partial \psi}{\partial x}(x_{\max}, y) = 0,$$

$$\psi(x, y_{\min}) = -1 \quad \text{and} \quad \psi(x, y_{\max}) = -1.$$

### 2.4.3 Boundary condition on the pressure

When the sample solution starts moving in response to an applied electric field, the fluid height in the input and output reservoir may change. This will impose a pressure gradient along the channel. Using a Dirichlet boundary condition, we specify the dimensionless pressure values at the input and output boundaries. A Neumann boundary condition is used for the pressure at the walls. Thus, the boundary conditions on $P$ are the similar to that used by Sidilkover & Ascher (1995).

$$P(x_{\min}, y) = P_0 \quad \text{and} \quad P(x_{\max}, y) = P_1,$$

$$\frac{\partial P}{\partial y}(x, y_{\min}) = 0 \quad \text{and} \quad \frac{\partial P}{\partial y}(x, y_{\max}) = 0,$$

where $P_0$ and $P_1$ are the pressures at the input and output reservoirs, respectively.

### 2.4.4 Boundary condition on the velocity field

We use a no-slip boundary condition on the walls, which is a good approximation. To determine the boundary condition at the input and output boundaries, we assume that the channel is infinitely long and we want to start from a position and truncate the channel at some other location. Taking this into consideration, we adopt a Neumann boundary condition at the input and output boundaries:

$$\frac{\partial \boldsymbol{v}}{\partial x}(x_{\min}, y) = 0 \quad \text{and} \quad \frac{\partial \boldsymbol{v}}{\partial x}(x_{\max}, y) = 0,$$

$$\boldsymbol{v}(x, y_{\min}) = 0 \quad \text{and} \quad \boldsymbol{v}(x, y_{\max}) = 0.$$

### 2.4.5 Boundary condition on the concentration field

For the concentration field, we use a Neumann boundary condition on the walls and a Dirichlet boundary condition at the input and output:

$$C(x_{\min}, y) = C_0, \quad C(x_{\max}, y) = C_1,$$

$$\frac{\partial C}{\partial y}(x, y_{\min}) = 0 \quad \text{and} \quad \frac{\partial C}{\partial y}(x, y_{\max}) = 0,$$

where $C_0$ and $C_1$ are the concentrations in the input and output reservoirs, respectively.

### 2.4.6 Boundary condition on the fluxes

It is also necessary to impose an additional boundary condition for fluxes in order to finite difference the momentum and concentration equations. A Neumann boundary condition is used on $\Gamma_x$ at the inlet and outlet boundaries and a Dirichlet condition is used on $\Gamma_y$ at the walls:

$$\frac{\partial \Gamma_x}{\partial x}(x_{\min}, y) = \frac{\partial \Gamma_x}{\partial x}(x_{\max}, y) = 0,$$

$$\Gamma_y(x, y_{\min}) = \Gamma_y(x, y_{\max}) = 0.$$

## 2.5 Conservation laws and the Kolmogorov hypothesis

In the limit of no forcing and dissipation, (2.23)–(2.25) possess four quadratic invariants: the energy (mean-squared velocity), the enstrophy (mean-squared vorticity), the mean-squared concentration, and the cross correlation of the vorticity and concentration fields. In Appendix B, these conserved quantities are defined and discussed in detail. The application of the Kolmogorov hypothesis to derive the spectrum of the mean-squared concentration is also discussed in Appendix B.

# Chapter 3

# DISCRETIZATION

## 3.1 Numerical grid

Since electro-osmosis obeys a nonlinear system of differential equations, it is advantageous to study the phenomenon numerically. Because of the underlying nonlinearity, exact analytical solutions to the governing equations of motion for fluid flow do not exist in most cases. Numerical computation can provide approximate solutions to the fully nonlinear model. A detailed discussion of a computational approach to fluid flow is not the aim of this study. Rather, we want to note that the constitutive continuum equations can never hope to be called exact and numerical simulations deal with some sort of discrete approximation to the continuum equation. The act of discretization may change not only the quantitative accuracy but also the qualitative behaviour of

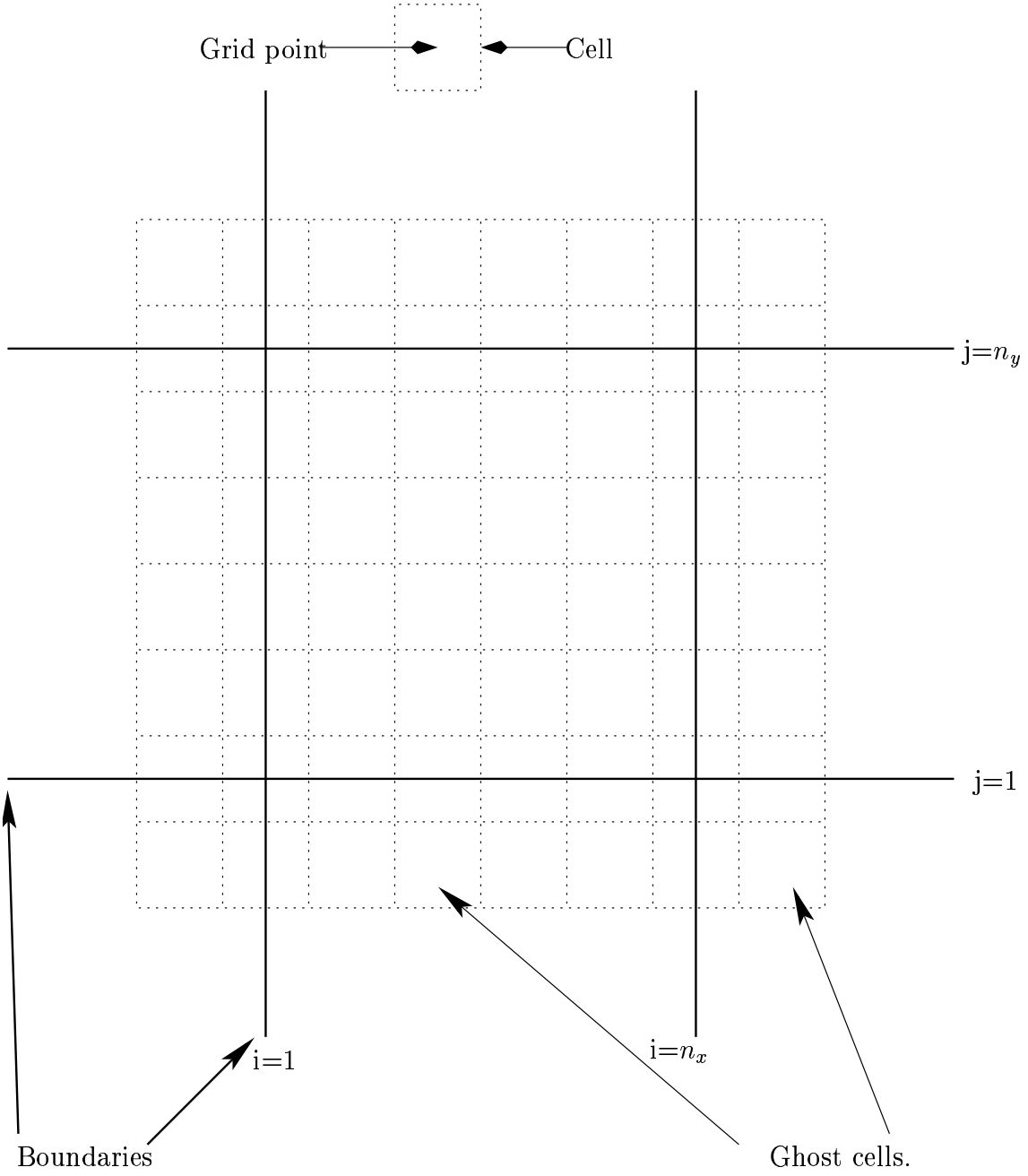


Figure 3.1: A schematic grid.

the equation. Also there is no uniquely defined form for a discrete approximation to the continuum equation. On the other hand there are few rigorous stability analyses, error estimates, or convergence proofs for a system of nonlinear partial differential equations (Roache 1972).

Let us sub-divide the computational domain into a finite number of sub-domains which we will call 'cells' and define a grid $\Omega_l$, where $l$ denotes the resolution of the grid. A suitable difference approximation to a differential operator can then be constructed on $\Omega_l$ by using Taylor series expansion. To construct a uniform grid $\Omega_l$ on the domain

$$\Omega = \{(x, y) : x_{\min} \leq x \leq x_{\max}, y_{\min} \leq y \leq y_{\max}\},$$

we define grid points $(x_i,\ y_i)$ as follows,

$$x_i = ih_x\ ,\ \ i = 1, 2, \ldots, n_x,$$

$$y_i = ih_y\ ,\ \ i = 1, 2, \ldots, n_y,$$

$$h_x = x_{i+1/2} - x_{i-1/2},$$

$$h_y = y_{i+1/2} - y_{i-1/2},$$

where $h_x$ is the length of a cell, $h_y$ is the width of a cell, $n_x$ is the number of cells in the $x$ direction and $n_y$ is the number of cells in the $y$ direction. In Fig. (3.1) we show a fine grid in the two-dimensional case, where the dotted lines correspond to the cell boundary. Let us now consider the initial-boundary value problem

$$\mathcal{L}_\Omega u = f_\Omega \quad \boldsymbol{x} \in \Omega,$$

$$\mathcal{L}_{\partial\Omega} u = f_{\partial\Omega} \quad \boldsymbol{x} \in \partial\Omega,$$

where $\partial\Omega$ is the boundary of the computational domain. The differential operators $\mathcal{L}_\Omega$ and $\mathcal{L}_{\partial\Omega}$ may depend both on time and space. Upon suitable discretization, we get a discrete set of equations on a grid $\Omega_l$ (Hackbusch 1985),

$$\mathcal{L}_{h_l} = f_l \quad x_i \in \Omega_l,$$

where

$$\mathcal{L}_{h_l} = \begin{pmatrix} \mathcal{L}_{\Omega_l} \\ \\ \mathcal{L}_{\partial\Omega_l} \end{pmatrix}.$$

In order to construct $\mathcal{L}_{h_l}$ , we need to discretize $\mathcal{L}_\Omega$ and $\mathcal{L}_{\partial\Omega}$ on each grid $\Omega_l$ both in space and time. Although a standard finite difference approximation to a derivative in a finite difference grid is second-order central in space, difficulties are encountered in handling passive advection. We have therefore developed a new method to model properly the advective term $\boldsymbol{v} \cdot \boldsymbol{\nabla} C$, where $C$ is a scalar field.

## 3.2 Spatial discretization

In order to solve a system of partial differential equations on a computer, we have to derive a discrete version of our continuous equations. In this section we will describe spatial discretization and obtain a semi-discrete version of the governing partial differential equations. It is convenient to write down the equation of motion in a flux-conservative form using the incompressibility condition and Laplace's equation for the external potential. We re-write the flux conservative version of (2.23)–(2.24)

below,

$$\frac{\partial v}{\partial t} + \boldsymbol{\nabla} \cdot (\boldsymbol{v}\boldsymbol{v}) = -\boldsymbol{\nabla} P + \nu_v \nabla^2 \boldsymbol{v} + \alpha\psi \boldsymbol{\nabla}\varphi, \tag{3.1}$$

$$\frac{\partial C}{\partial t} + \boldsymbol{\nabla} \cdot [(\boldsymbol{v} - \mu \boldsymbol{\nabla}\varphi)\, C] = \nu_c \nabla^2 C. \tag{3.2}$$

In a compact notation the equations take the form

$$\frac{\partial \boldsymbol{U}}{\partial t} + \boldsymbol{\nabla} \cdot \boldsymbol{\Gamma} = \boldsymbol{\nu} \nabla^2 \boldsymbol{U} + \boldsymbol{f}(\boldsymbol{U}),$$

where $\boldsymbol{U}$ , $\boldsymbol{\Gamma}$ , $\boldsymbol{\nu}$ , $\boldsymbol{f}$ are defined as follows

$$\boldsymbol{U} = \begin{bmatrix} v_x \\ v_y \\ C \end{bmatrix}, \tag{3.3}$$

$$\boldsymbol{\nu} = \begin{bmatrix} \nu_v & 0 & 0 \\ 0 & \nu_v & 0 \\ 0 & 0 & \nu_c \end{bmatrix},$$

$$\boldsymbol{f} = \begin{bmatrix} \alpha\psi \dfrac{\partial \varphi}{\partial x} - \dfrac{\partial P}{\partial x} \\ \alpha\psi \dfrac{\partial \varphi}{\partial y} - \dfrac{\partial P}{\partial y} \\ 0 \end{bmatrix},$$

$$\boldsymbol{\Gamma} = \begin{bmatrix} \Gamma_{v_x} \\ \Gamma_{v_y} \\ \Gamma_C \end{bmatrix},$$

$$\Gamma_{v_x} = \begin{bmatrix} v_x v_x \\ v_y v_x \end{bmatrix},$$

$$\Gamma_{v_y} = \begin{bmatrix} v_x v_y \\ \\ v_y v_y \end{bmatrix},$$

$$\Gamma_C = \begin{bmatrix} v_x C - \mu \dfrac{\partial \varphi}{\partial x} C - \mu \dfrac{\partial \varphi}{\partial y} C \\ \\ v_y C - \mu \dfrac{\partial \varphi}{\partial x} C - \mu \dfrac{\partial \varphi}{\partial y} C \end{bmatrix}.$$

The velocity, concentration, pressure, potential, and fluxes are approximated at the centroid of each cell as cell-averaged quantities. We will be using a second-order accurate centered-in-space finite difference formula to evaluate the derivatives on the numerical grid. For example, for any function $F(x)$, we evaluate

$$\left(\frac{\partial F}{\partial x}\right)_i = \frac{F_{i+1} - F_{i-1}}{2h_x}, \tag{3.4}$$

Generally, second derivatives with respect to $x$ are evaluated to second-order accuracy:

$$\left(\frac{\partial F}{\partial x}\right)_i = \frac{F_{i+1/2} - F_{i-1/2}}{h_x},$$

$$\left(\frac{\partial^2 F}{\partial x^2}\right)_i = \frac{\left(\dfrac{\partial F}{\partial x}\right)_{i+1/2} - \left(\dfrac{\partial F}{\partial x}\right)_{i-1/2}}{h_x}, \tag{3.5}$$

$$= \frac{F_{i+1} - 2F_i + F_{i-1}}{h_x^2}. \tag{3.6}$$

Difficulties can arise in applying these formulae to model practical problems on a computer. We can handle these troubles by appealing to the underlying physics.

### 3.2.1 Discretization of the fluxes

We calculate derivatives of fluxes directly with the centered difference formula given by (3.4)

$$\left(\frac{\partial \Gamma}{\partial x}\right)_{i,j} = \frac{\Gamma_{i+1,j} - \Gamma_{i-1,j}}{2h_x},$$

$$\left(\frac{\partial \Gamma}{\partial y}\right)_{i,j} = \frac{\Gamma_{i,j+1} - \Gamma_{i,j-1}}{2h_y}.$$

### 3.2.2 Discretization of a Laplacian operator

We adopt the usual second-order formula (3.6) to evaluate the Laplacian operator. Hence the finite difference formula for the Laplacian takes the form

$$\nabla^2 u = \frac{u_{i+1,j} - 2u_{i,j} + u_{i-1,j}}{h_x^2} + \frac{u_{i,j+1} - 2u_{i,j} + u_{i,j-1}}{h_y^2}. \tag{3.7}$$

This compact finite difference formula is used to solve (2.26) and (2.27).

### 3.2.3 Finite differencing of the pressure term

The pressure gradient term that appears in the momentum equation causes additional difficulties when one attempts to solve the Navier–Stokes equation numerically (Tannehill *et al.* 1997). First of all, one needs to decouple the pressure term from the original equation and evaluate the pressure in each cell. This pressure is then

used as a source term for the original equation (Tannehill *et al.* 1997). Pressure acts in such a way as to keep each parcel of fluid incompressible. It can be shown that pressure varies linearly with the length of the channel in the case of channel flow (Kundu 1990). We can calculate the pressure gradient with a second-order central finite difference formula:

$$\left(\frac{\partial P}{\partial x}\right)_{i,j} = \frac{P_{i+1,j} - P_{i-1,j}}{2h_x},$$

$$\left(\frac{\partial P}{\partial y}\right)_{i,j} = \frac{P_{i,j+1} - P_{i,j-1}}{2h_y}.$$

Since the pressure Poisson equation is derived by taking the divergence of the momentum equation, the Laplacian in this case should be treated as a divergence of a gradient. We adopt the following formula for the Laplacian that appears in the pressure Poisson equation,

$$\begin{aligned}
\nabla^2 P &= \left[\frac{\partial}{\partial x}\left(\frac{\partial P}{\partial x}\right)\right]_{i,j} + \left[\frac{\partial}{\partial y}\left(\frac{\partial P}{\partial y}\right)\right]_{i,j} \\
&= \frac{\left(\frac{\partial P}{\partial x}\right)_{i+1,j} - \left(\frac{\partial P}{\partial x}\right)_{i-1,j}}{2h_x} + \frac{\left(\frac{\partial P}{\partial y}\right)_{i,j+1} - \left(\frac{\partial P}{\partial y}\right)_{i,j-1}}{2h_y} \\
&= \frac{P_{i+2,j} - 2P_{i,j} + P_{i-2,j}}{4h_x^2} + \frac{P_{i,j+2} - 2P_{i,j} + P_{i,j-2}}{4h_y^2}.
\end{aligned}$$

This differencing is second-order accurate and central in space. It differs from the compact differencing of the Laplacian in that it keeps the velocity field divergence free; this ensures that the advective term in the momentum equation will conserve energy and enstrophy if there is no forcing and dissipation (see Appendix B). Let us write down the spatially discretized momentum equation in the absence of forcing

and dissipation.

$$\frac{\partial \boldsymbol{v}_{i,j}}{\partial t} + \boldsymbol{v}_{i,j} \cdot \boldsymbol{\nabla}_1 \boldsymbol{v}_{i,j} = -\boldsymbol{\nabla}_1 P, \tag{3.8}$$

where the discrete operator $\boldsymbol{\nabla}_1$ is defined by

$$\boldsymbol{\nabla}_1 F = \frac{F_{i+1,j} - F_{i-1,j}}{2h_x}\hat{x} + \frac{F_{i,j+1} - F_{i,j-1}}{2h_y}\hat{y}.$$

If we use the non-compact discretization

$$\boldsymbol{\nabla}_1 \cdot [\boldsymbol{v}_{i,j} \cdot \boldsymbol{\nabla}_1 \boldsymbol{v}_{i,j} + \boldsymbol{\nabla}_1 P] = 0 \tag{3.9}$$

to calculate the pressure, then (3.8) will preserve the incompressibility of the flow:

$$\boldsymbol{\nabla}_1 \cdot \boldsymbol{v}_{i,j} = 0.$$

This in turn guarantees that the energy and enstrophy are conserved in the limit of no dissipation or forcing (see Appendix B).

To compare these two discretizations for the pressure equation, we calculate two quadratic invariants, energy and enstrophy, using a fifth-order Runge–Kutta integrator. It is found that both energy and enstrophy are conserved to high accuracy only if the non-compact formula is used to calculate the pressure. We present results from our numerical simulation in Figs. 4.1 and 4.2 to show the necessity of using this non-compact finite difference formula for the Laplacian of the pressure.

### 3.2.4 Semi-discrete version of the governing equations

A semi-discrete approximation to (2.23) and (2.24) is given by

$$\frac{\partial \boldsymbol{U}_{i,j}}{\partial t} + \frac{\boldsymbol{\Gamma}_{i+1,j} - \boldsymbol{\Gamma}_{i-1,j}}{2h_x} + \frac{\boldsymbol{\Gamma}_{i,j+1} - \boldsymbol{\Gamma}_{i,j-1}}{2h_y} = \boldsymbol{\nu}\nabla^2 \boldsymbol{U}_{i,j} + \boldsymbol{f}_{i,j}$$

where $\boldsymbol{U}_{i,j}$ is a compact notation for $\boldsymbol{U}(ih_x, jh_y)$ and $ih_x$, $jh_y$ are the values of $x$ and $y$ at grid points $i$ and $j$. In order to evaluate $\boldsymbol{f}_{i,j}$ we also need to solve three elliptic differential equations of the following form

$$\nabla^2 \boldsymbol{u} = \boldsymbol{f}(u),$$

where

$$\boldsymbol{u} = \begin{bmatrix} P \\ \varphi \\ \psi \end{bmatrix},$$

$$\boldsymbol{f}(u) = \begin{bmatrix} \boldsymbol{\nabla} \cdot [\alpha\psi \boldsymbol{\nabla}\varphi - v \cdot \boldsymbol{\nabla} v] \\ 0 \\ \kappa^2 \psi \end{bmatrix}.$$

## 3.3 Temporal discretization

The temporal discretization of hyperbolic partial differential equations is a little trickier. A time derivative can be discretized by using a forward difference formula in the

following way:

$$\frac{\partial u}{\partial t}|_n = \frac{u^{n+1} - u^n}{\tau}.$$

The advantage of using a forward difference formula is that one can predict quantities for the future by using information only from the present. The temporal discretization should be handled very carefully. In the case of a pure advection equation, the spatial discretization of the advective term that is described in the previous section may introduce an unexpected instability in the numerical scheme. To avoid such a difficulty, one may look for an alternate spatial discretization that provides stability. It has been pointed out that the instability that is encountered in solving an advection equation on a computer arises not only because of the discretization of the advective term, but also because the time scale of this term is not being properly modeled. This has been explained in Press *et al.* (1997, and refs. therein) and Tannehill *et al.* (1997).

### 3.3.1 Stability problem with the advective derivative

Let us consider a one-dimensional linear advection equation

$$\frac{\partial \Psi}{\partial t} + v\frac{\partial \Psi}{\partial x} = 0.$$

A forward time centered space representation of the above equation is given by

$$\frac{\Psi_i^{n+1} - \Psi_i^n}{\tau} = v_i^n \frac{\Psi_{i+1}^n - \Psi_{i-1}^n}{2h},$$

where $\Psi_i^n$ stands for $\Psi(x_i, t_n)$ and $x_i$ and $t_n$ denote the $i$-th grid point and $n$-th time step, respectively.

To realize how this discrete equation approximates the original continuous equation, a differential equation can be obtained from the discrete equation in the following form (Tannehill *et al.* 1997, and refs. therein),

$$\frac{\partial \Psi}{\partial t} + v\frac{\partial \Psi}{\partial x} = -\frac{v^2\tau}{2}\frac{\partial^2 \Psi}{\partial x^2} + O(\tau^2, h^2).$$

This is the partial differential equation that we are actually solving instead of the original one. The leading-order term on the right hand side is in the form of a negative diffusion and this is the source of instability since a diffusion coefficient has always to be positive. To address this problem, the alternate approach is to change the spatial discretization in the following way (Press *et al.* 1997):

$$\frac{\Psi_i^{n+1} - \Psi_i^n}{\tau} = \begin{cases} -v_i^n \frac{\Psi_i^n - \Psi_{i-1}^n}{h} & \text{if} \quad v_i^n > 0, \\ -v_i^n \frac{\Psi_{i+1}^n - \Psi_i^n}{h} & \text{if} \quad v_i^n < 0. \end{cases}$$

This is the first–order upwind method. It is stable only if the Courant condition

$$C_u = \frac{v\tau}{h} \leq 1$$

is satisfied. In this case we obtain

$$\frac{\partial \Psi}{\partial t} + v\frac{\partial \Psi}{\partial x} = \frac{vh_x}{2}(1 - C_u)\frac{\partial^2 \Psi}{\partial x^2} + O(\tau, h^2).$$

The upwind method makes the scheme stable by adding a velocity-dependent viscosity to the original equation. The coefficient of the leading-order even derivative term in

the truncation error measures the extra diffusion imposed by the numerical method (Tannehill *et al.* 1997). The coefficient of the leading term on the right-hand side of the above equation will be small if a very fine grid is used. However, if there is a small viscosity in the original equation, which is the case for an advection-dominated flow, the second-order central formula could provide a stable solution for a fine grid with a sufficiently small time step (Tannehill *et al.* 1997). If the Courant limit is violated, the leading term again becomes negative, making the scheme unstable. The artificially imposed viscosity dampens the solution rapidly and we fail to accomplish our original goal. From this simple example, it is seen that viscosity plays an important role in removing numerical instability. It is clear that changing the spatial discretization is not the best way to handle an advective derivative. It is also important to note that if there is enough viscosity in the original equation to defeat the negative viscosity that is seen in the previous equation, a second-order central approximation to the advective derivative would still provide a stable numerical scheme. Our temporal discretization is based on this observation. Since we are dealing with electro-osmotic flow, the Reynolds number in this case is usually small (Patankar & Hu 1998). That is, for the experimental scales and velocities we are interested in, the viscous forces dominate the inertial forces. We have seen that the numerical scheme has problems if there is not enough viscosity in the original equation. One way of solving this problem is to treat the advective term and the viscous term separately. Since (2.23) has sufficient viscosity for an Eulerian method to be stable, we concentrate the nonlinearity in the

advective term explicitly on the right-hand side as a source term, and for the viscous term we use a Crank–Nicholson method (Richtmyer & Morton 1957; Jia 1998). The discretized momentum equation is

$$\frac{\boldsymbol{v}_{i,j}^{n+1} - \boldsymbol{v}_{i,j}^{n}}{\tau} = \frac{\nu_v}{2}\nabla^2 \left(\boldsymbol{v}_{i,j}^{n+1} + \boldsymbol{v}_{i,j}^{n}\right) + \boldsymbol{S}_{i,j}^{n},$$

where we have incorporated the advective derivative, pressure force and body force explicitly as a source in $\boldsymbol{S}$. This in turn requires the solution of the linear system of equations

$$\left(\boldsymbol{I} - \frac{\nu_v \tau}{2}\nabla^2\right) \boldsymbol{v}_{i,j}^{n+1} = \left(\boldsymbol{I} + \frac{\nu_v \tau}{2}\nabla^2\right) \boldsymbol{v}_{i,j}^{n} + \tau \boldsymbol{S}(\boldsymbol{v}_{i,j}^{n}), \tag{3.10}$$

*i.e.*,

$$\boldsymbol{\mathcal{L}}(\tau)\boldsymbol{v}_{i,j}^{n+1} = \boldsymbol{\mathcal{L}}(-\tau)\boldsymbol{v}_{i,j}^{n} + \tau \boldsymbol{S}(\boldsymbol{v}_{i,j}^{n}), \tag{3.11}$$

where the operator $\boldsymbol{\mathcal{L}}$ is defined by

$$\boldsymbol{\mathcal{L}}(\tau) = \boldsymbol{I} - \frac{\nu_v \tau}{2}\nabla^2. \tag{3.12}$$

The linear system (3.11) can be solved using the iterative method described in the next section.

For the concentration equation, we treat advection and diffusion separately. Let $\tilde{C}$ denote the solution of the pure advection equation

$$\frac{\partial \tilde{C}}{\partial t} + \boldsymbol{v} \cdot \boldsymbol{\nabla} \tilde{C} = 0,$$

with the initial condition

$$\tilde{C}(\boldsymbol{x}, 0) = C_0.$$

Since the velocity field is computed from the momentum equation, the advection can be done easily in a Lagrangian frame. We can then combine advection and diffusion in the following way:

$$\frac{C_{i,j}^{n+1} - \tilde{C}_{i,j}^{n}}{\tau} = \frac{\nu_c}{2}\nabla^2 \left( C_{i,j}^{n+1} + \tilde{C}_{i,j}^{n} \right). \tag{3.13}$$

This procedure is known as operator splitting (Ames 1977; Press *et al.* 1997). Equation (3.13) requires the solution of another linear system of equations, which is similar to (3.10). Thus, in a compact notation we can write down the following linear system of equations,

$$\boldsymbol{\mathcal{L}}(\tau)\boldsymbol{U}^{n+1} = \boldsymbol{\mathcal{L}}(-\tau)\tilde{U}^{n} + \tau \boldsymbol{S}(\tilde{U}^{n}), \tag{3.14}$$

where $\boldsymbol{U}$ is given by (3.3), and the source vector $\boldsymbol{S}$ is given by

$$\boldsymbol{S} = \begin{bmatrix} S_{v_x} \\ S_{v_y} \\ 0 \end{bmatrix}.$$

For the momentum equation, we treat both advection and diffusion in an Eulerian frame. Thus, $\tilde{\boldsymbol{v}}^n = \boldsymbol{v}^n$.

The overall semi-implicit algorithm is summarized below:

1. Calculate the source $\boldsymbol{S}$ for each equation.

2. Evaluate the quantity $\tilde{\boldsymbol{U}}^n$.

3. Evaluate the expression

$$\boldsymbol{\mathcal{L}}(-\tau)\tilde{\boldsymbol{U}}^n + \tau \boldsymbol{S}(\tilde{\boldsymbol{U}}^n).$$

4. Invert the operator $\boldsymbol{\mathcal{L}}(\tau)$ to get

$$\boldsymbol{U}^{n+1} = \boldsymbol{\mathcal{L}}^{-1}(\tau)\left(\boldsymbol{\mathcal{L}}(-\tau)\tilde{\boldsymbol{U}}^n + \tau \boldsymbol{S}(\tilde{\boldsymbol{U}}^n)\right)$$

for the new time level.

A multigrid solver, developed by Bowman *et al.* (2000), is used to invert the operator $\boldsymbol{\mathcal{L}}$.

## 3.4 Multigrid Poisson solver

A linear system of equations arises once the time-dependent partial differential equations are discretized both in space and time. The Helmholtz equation $\boldsymbol{\mathcal{L}}\boldsymbol{U} = f$, where $\boldsymbol{\mathcal{L}}$ is defined by (3.12), can be solved using the multigrid solver developed by Bowman *et al.* (2000). Because the multigrid method is described in detail by Hackbusch (1985), Briggs (1987), Press *et al.* (1997), Tannehill *et al.* (1997), we provide only a short description of this efficient iterative method.

A number of iterative methods do exist to solve a Poisson and Helmholtz equations. Without going into details of the traditional iterative methods, usually termed relaxation methods, we note that classical iterative methods converge very slowly

when solving large linear systems and the convergence rate depends on the number of grid points in the computational domain (Press *et al.* 1997). A multigrid algorithm offers convergence rates that are independent of the number of grid points and is very effective for solving large scale computation-intensive problems (Briggs 1987). The algorithm iterates on a hierarchy of consecutively coarser and coarser grids until convergence is reached. Considerable computational time is saved by exploiting the fast convergence of relaxation methods on the coarse grids.

The construction of a multigrid iteration is based on the observation that relaxation converges very slowly as $h \rightarrow 0$, where $h$ is the grid size. In Fourier space, smooth components of the error (low wavenumbers) are only slightly reduced in amplitude; non-smooth components (high wavenumbers) are reduced by a large amount in each iteration. Multigrid iteration exploits the fact that a component which is smooth on a fine grid appears as a non-smooth function on a coarser grid. The implementation of a complete multigrid iteration requires **smoothing** the error, **restriction** of the defect from the fine to the coarse grid, **solving** the coarse grid error equation, and **interpolation** of the coarse grid error to the fine grid. However solving the coarse grid error equation is not a straight-forward task. Depending on the number of grid points in the coarse grid, one moves recursively to coarser and coarser grids until the coarse grid solution is achieved exactly or easily. Smoothing may have two steps: pre-smoothing and post-smoothing. Pre-smoothing smoothes the non-smooth component of error before restricting to the coarser grid. Post-smoothing does the

same after interpolation. A typical multigrid iteration, starting with the finest grid, can be described as follows:

- Start with any initial guess on the given grid.
- Smooth the error on the grid.
- Restrict the defect to a coarser grid.
- Solve the coarse grid error equation by applying the above three steps recursively.
- Interpolate the error from the coarsest grid to a finer grid, obtaining the smooth error in the finer grid, and repeat the interpolation recursively until the finest grid is reached.
- Update the initial guess in the finest grid.

This completes one cycle of a multigrid iteration. We adopt this algorithm to solve the three equations (2.25, 2.26, 2.27) and the linear system of equations (3.14) that arises after discretization both in space and time.

## 3.5 Parcel advection

The basic idea of the parcel advection algorithm is based on Lagrangian coordinates. For simplicity, let us consider the one-dimensional linear advection equation which,

in Eulerian notation, is usually written as

$$\frac{\partial C(x,t)}{\partial t} + u\frac{\partial C(x,t)}{\partial x} = 0. \tag{3.15}$$

This equation may also be written using Lagrangian notation as

$$\frac{d}{dt}C(\xi(t),t) = 0, \tag{3.16}$$

where the Lagrangian trajectory, $\xi(t)$, is given by the solution of

$$\frac{d}{dt}\xi(t) = u.$$

Equation (3.15) can then be obtained from (3.16) by applying the Chain Rule. Equation (3.16) states that the scalar $C(x,t)$ is constant in time along a fluid path or trajectory, $\xi(x(t),t)$. If $C(x,t)$ is known at some reference time and location on the path, this value is propagated along the trajectory. The trajectory described by (3.15) is given by

$$\xi(x(t+\tau),t) - \xi(x(t),t) = \int_t^{t+\tau} u\,dt \approx u\tau$$

if $\tau$ is sufficiently small. Thus if a scalar quantity is evaluated at $\xi(x(t),t)$, the quantity will be advected in a time interval $\tau$ to the location $\xi(x(t+\tau),t) = \xi(x(t),t)+u\tau$. Having this fundamental idea in mind, let us adopt a uniform square grid and model the fluid as a collection of square fluid parcels, each of the same size as a grid cell. Initially these parcels each occupy exactly one cell of the grid and contain the concentration initially prescribed to that cell. There is a mean velocity associated with each parcel, which is calculated as an area-weighted average of the fluid velocities of

the cells it overlaps. Initially it overlaps just one cell, but it could overlap as many as four cells. This mean velocity is used to advect the cell undistorted, so that after each time step, the parcel is still square. The advection of a fluid parcel is shown in Fig. (3.2)(b).

### 3.5.1 Advection stage

In Fig. (3.2)(a), we show a particular parcel, which initially occupies one cell in the grid. The velocity and concentration of the parcel is the same as that of the cell. With this velocity the parcel is advected along the trajectory and may overlap as many as four cells. The velocity associated with the parcel is determined as an area-weighted average velocity of the velocities of the overlapping cells. Let the initial velocity $\boldsymbol{v}$ of this parcel be equal to the velocity at the centroid of the cell that the parcel initially occupies. In time $\tau$, the parcel is advected to the position shown in Fig. 3.2(b). After each advection, the parcel gains velocity from the overlapping cells. In Fig. 3.3, we show the new position of the parcel and the areas of the overlapping cells. We calculate the new position of the parcel with the Euler step

$$\boldsymbol{\xi}^{n+1} = \boldsymbol{\xi}^n + \boldsymbol{v}\tau.$$

That is, the coordinates of the centroid of the parcel, $(\xi_x^n, \xi_y^n)$, after $n$ time steps is given by

$$\xi_x^n = \xi_x^{n-1} + v_x\tau,$$

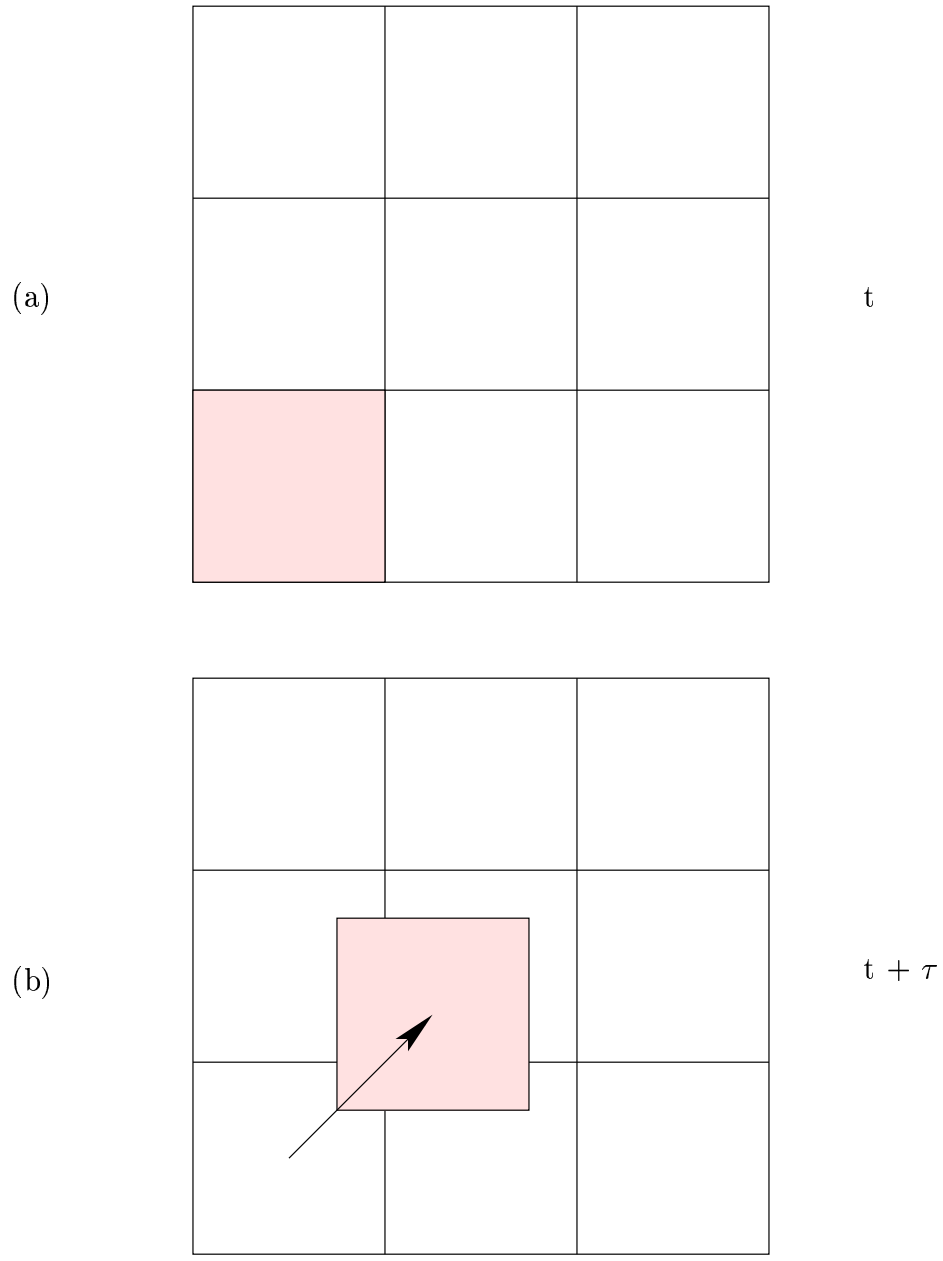


Figure 3.2: Advection of a parcel.

$$\xi_y^n = \xi_y^{n-1} + v_y \tau,$$

where $(\xi_x^{n-1}, \xi_y^{n-1})$ is the previous position of the parcel.

### 3.5.2 Calculating the area of the overlapping cells

Let us denote the overlapping areas by $A_1$, $A_2$, $A_3$, and $A_4$ as shown in Fig. 3.3. We calculate the overlapping areas from the following formulae

$$A_1 = \left( h_x \left\lfloor \frac{\xi_x^n}{h_x} \right\rfloor + h_x - \xi_x^n \right) \left( h_y \left\lfloor \frac{\xi_y^n}{h_y} \right\rfloor + h_y - \xi_y^n \right),$$

$$A_2 = \left( \xi_x^n - \left\lfloor \frac{\xi_x^n}{h_x} \right\rfloor \right) \left( h_y \left\lfloor \frac{\xi_y^n}{h_y} \right\rfloor + h_y - \xi_y^n \right),$$

$$A_3 = \left( h_x \left\lfloor \frac{\xi_x^n}{h_x} \right\rfloor + h_x - \xi_x^n \right) \left( \xi_y^n - \left\lfloor \frac{\xi_y^n}{h_y} \right\rfloor \right),$$

$$A_4 = \left( \xi_x^n - \left\lfloor \frac{\xi_x^n}{h_x} \right\rfloor \right) \left( \xi_y^n - \left\lfloor \frac{\xi_y^n}{h_y} \right\rfloor \right).$$

### 3.5.3 Area-weighted average velocity

Assume that the parcel now overlaps four cells. The velocities of these cells are $v_1$, $v_2$, $v_3$, and $v_4$, as shown in Fig. 3.2(d). The new velocity $\boldsymbol{v}$ of a parcel is then calculated according to

$$v^n = \frac{\sum_{i=1}^{4} A_i \, v_i^{n-1}}{\sum_{i=1}^{4} A_i}.$$

With this new velocity, the parcel is advected one time step and the procedure is repeated.

### 3.5.4 Contribution of concentration to overlapping cells

Once a parcel is advected, it distributes the concentration that it carries among the overlapping cells. This concentration is distributed among the overlapping cells according to the overlapped areas. If the parcel overlaps an area $A_i$ of a cell, the amount of concentration, $A_i C/A$, where $A$ is the area of the cell and $C$ is the concentration of the advected parcel, will be distributed to that cell.

### 3.5.5 Parcel injection

At the very beginning of a run, each cell in the grid has one parcel of fluid. When a parcel is advected from a boundary cell into the computational domain, that cell requires another parcel to fill the place of an advected parcel. This is done by parcel injection. Since we have no-slip boundary conditions at the wall, no parcel will try to cross the wall. Once a parcel reaches a cell on the wall, it will achieve a zero velocity in the direction normal to the wall and will not be able to cross the wall boundary. On the out-flow boundary, parcels may freely leave the domain. On the in-flow boundary, the parcel advection code always assumes an infinite reservoir of input. When a parcel advances into the domain, the in-flow boundary cell gets a parcel from the input reservoir.

### 3.5.6 Parcel source

The algorithm described above can been generalized to incorporate parcel diffusion and other sources or sinks. The sources are first calculated on an Eulerian grid (*e.g.* using the Crank–Nicholson method described in Sec. 4.1.3). Just prior to advecting each parcel, the parcels in a given cell are given a contribution from the sources in the cells they overlap, weighted by the relative overlapping areas. When advecting a non-negative scalar such as a concentration, it is important to ensure that the concentration does not become negative. The parcels, with their updated concentration values, are then advected as usual.

## 3.6 Implementation of the boundary conditions

In order to solve the discretized equations, we need to implement the proper boundary conditions. We have described different boundary conditions that we need to apply in our numerical simulation. One needs to be careful in implementing boundary conditions when the simulation requires a sequence of grids. We add one more layer of cells in each direction of the grid, which we call ghost cells. An extra layer of cells are necessary to impose a Neumann boundary condition. We call this type of grid a Neumann grid. To incorporate Dirichlet type boundary conditions we do not need ghost cells since quantities are known at the boundary in this case. However, our

system of equations consists of different differential equations and different types of boundary conditions have to be used. One way of doing this is to use different type of grids. Since we need to use both type of boundary conditions at the same time, it is convenient to impose all the boundary conditions on the same type of grid.

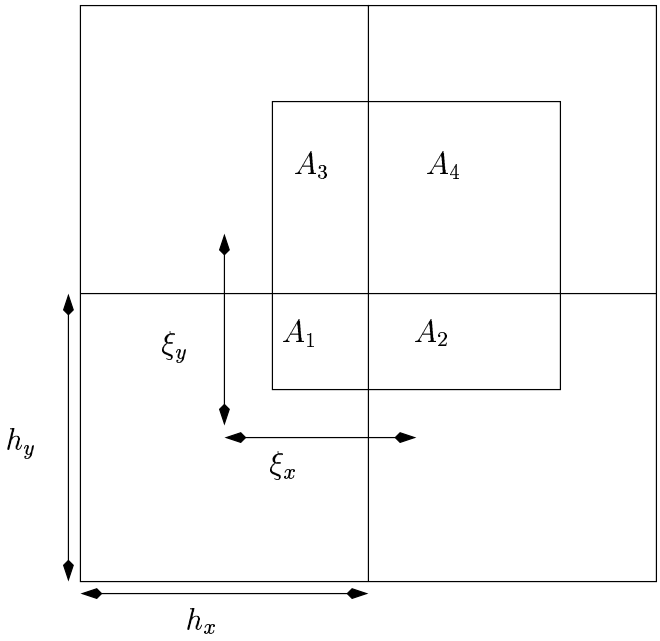


Figure 3.3: Contribution of a parcel to overlapping cells.

# Chapter 4

# NUMERICAL ANALYSIS AND RESULTS

## 4.1 Numerical solvers

In order to implement the algorithm described in the previous chapter, we have developed a C$^{++}$ module for the general purpose, object-oriented, initial value code `TRIAD`. Triad provides general facilities for parameter input, parsing, generic integration algorithms, dynamic time stepping, and a restart facility. One important step of our numerical scheme is to invert a Poisson equation for the pressure. Another computationally expensive step is to invert the Crank–Nicholson linear system. We have successfully developed a new scheme to handle passive advection without introducing

artificial diffusion.

### 4.1.1 Numerical simulation parameters

Here, we evaluate all of the non-dimensional parameters that are described earlier in Sec. 2.3.1. These parameters depend on various scales. The non-dimensional parameters have been evaluated from characteristic length and velocity scales based on typical laboratory experiments (Crabtree *et al.* 2000). We summarize below the characteristic scales and the non-dimensional parameters used in our numerical experiments.

$$\text{Length scale,} \quad h = 5 \times 10^{-5}\text{m},$$

$$\text{Length of the channel,} \quad H = 20h = 1 \times 10^{-3}\text{m},$$

$$\text{Velocity scale,} \quad U = 1 \times 10^{-3}\text{m/s},$$

$$\text{Pressure scale,} \quad \rho U^2 = 10^{-3}\,\text{Pa},$$

$$\text{Applied voltage at the input,} \quad \Phi_H = 70\text{V},$$

$$\text{Applied pressure at the input,} \quad P_0 = 120 \times \rho U^2,$$

$$\text{Kinematic viscosity of water,} \quad \nu = 10^{-6}\text{m}^2/\text{s},$$

$$\text{Diffusion coefficient,} \quad D = 10^{-11}\text{m}^2/\text{s},$$

$$\text{Electrophoretic mobility,} \quad \tilde{\mu} = 1.4 \times 10^{-8}\text{m}^2/\text{Vs},$$

$$\text{Zeta potential,} \quad \zeta = 0.1\text{V},$$

$$\text{Temperature,} \quad T = 300\,\text{K},$$

$$\text{Permitivity of water,} \quad \epsilon = 80.4 \times 8.85 \times 10^{-12}\ \text{C}^2/(\text{Nm}^2),$$

$$\text{Ion density,} \quad n = 34 \times 10^{-6}\ \text{mole/m}^3,$$

$$\text{Debye layer thickness,} \quad \lambda_D = 2.4 \times 10^{-6}\,\text{m},$$

$$\text{Computational grid,} \quad 1025 \times 65.$$

The thickness of the Debye layer is typically $(1 - 100)$nm, which can not be resolved in the numerical grid unless the grid size is very small. We use a value of ion density $n$ that produces a Debye layer such that it can be resolved in the numerical simulation.

The values for the dimensionless parameters that are defined in section 2.3.1 are

$$\nu_v = 20,$$

$$\nu_c = 2 \times 10^{-4},$$

$$\alpha = 9 \times 10^5,$$

$$\kappa^2 = 4.4 \times 10^2,$$

$$\mu = 20.$$

### 4.1.2 Pressure Poisson solver

As described in Sec. 3.2.3, the role of pressure in maintaining the incompressibility of the velocity field is respected by carefully discretizing the pressure Poisson equation.

Inverting the discrete Poisson equation is one of the more expensive computational steps because the pressure field has to be computed at each time step to enforce the incompressibility condition. The discrete Poisson equation is solved using a multigrid Poisson solver. The pressure solver is found to be convergent in 100 iterations on the very first time step with a computational grid of $1025 \times 65$, where the aspect ratio of the channel is $20 : 1$. In each of the subsequent time steps, convergence is achieved in ten iterations because the solver is initialized with the pressure values that were computed in the previous time step, providing an excellent initial guess for the current iteration. It is shown shown in Appendix B.1 that the energy and the enstrophy are conserved in the absence of forcing and dissipation. To test this numerically, (2.23) was solved without forcing and dissipation using a fifth order Runge-Kutta integrator. In Fig. 4.1 and Fig. 4.2, the numerically calculated energy and enstrophy is plotted. Discretization of the pressure Poisson equation using the non-compact formula is thus seen to conserve both energy and enstrophy to high accuracy. Accurate calculation of the energy and enstrophy is very desirable in computational fluid dynamics, since these two quantities are thought to be of fundamental importance in the cascade dynamics. For the simple case of two-dimensional flow in a rectangular channel, the mean pressure varies linearly with the length of the channel (Kundu 1990). The result from the pressure-Poisson solver is shown in Fig. 4.3.

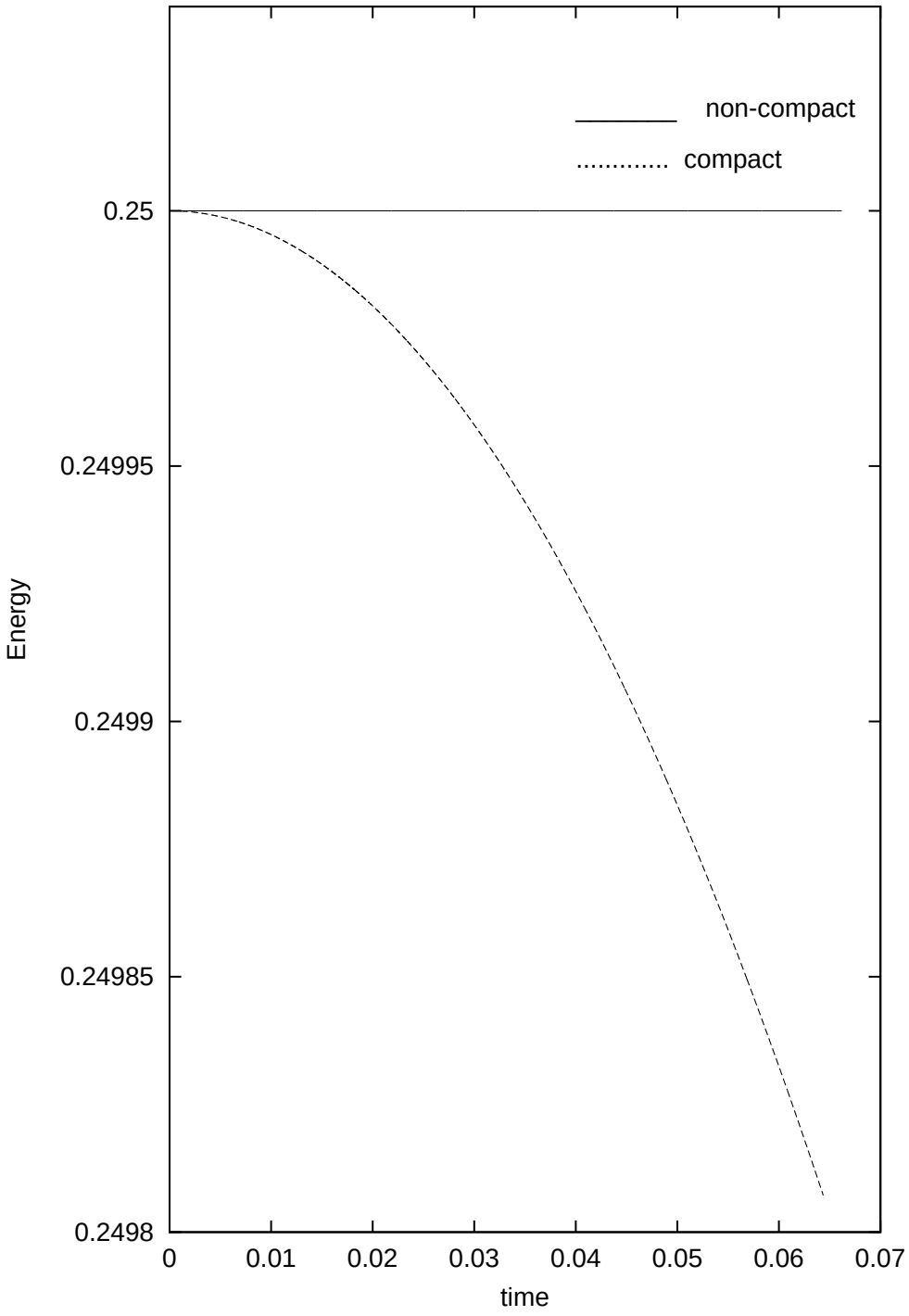


Figure 4.1: Conservation of energy for compact and non-compact pressure formulation.

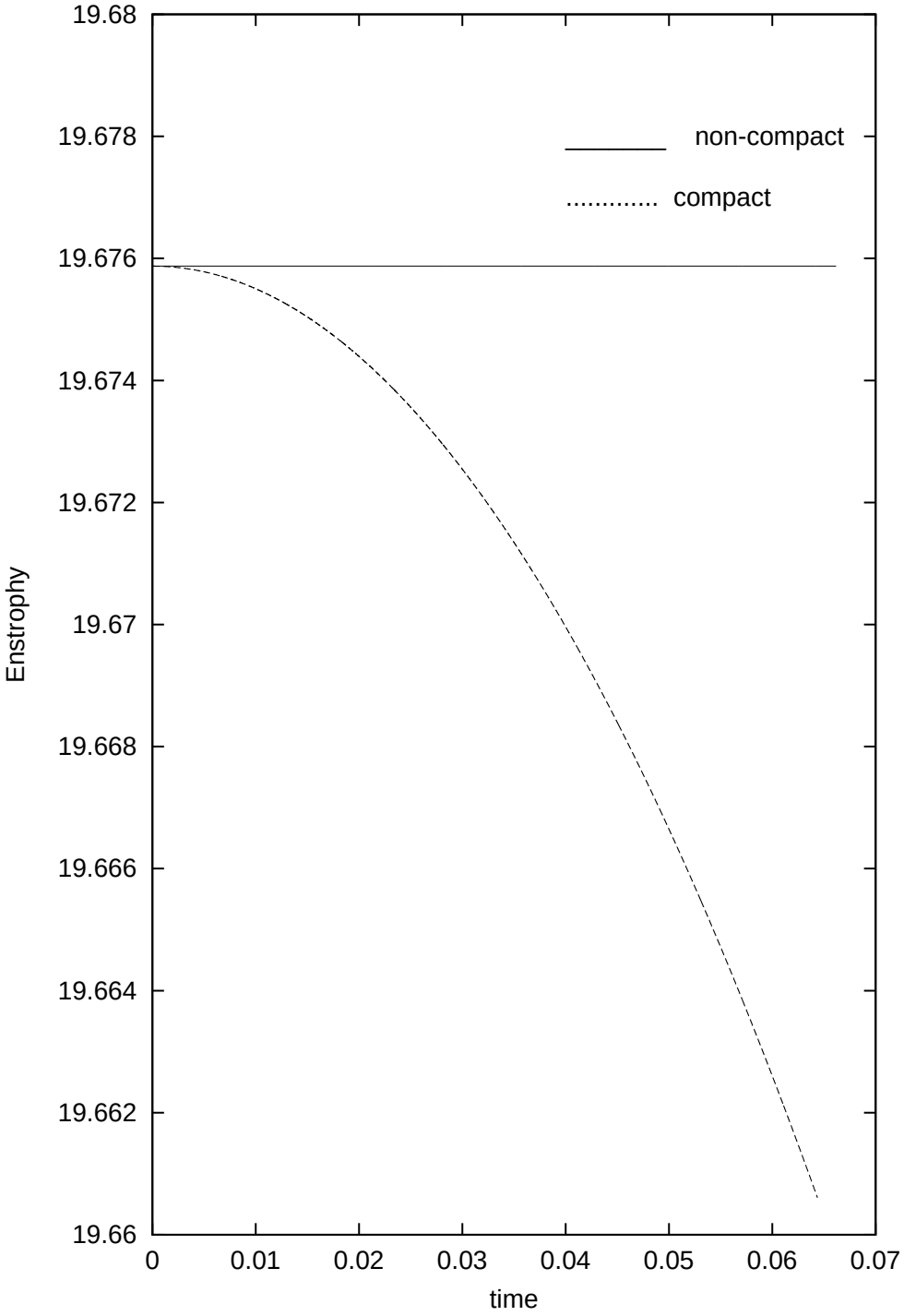


Figure 4.2: Conservation of enstrophy for compact and non-compact pressure formulation.

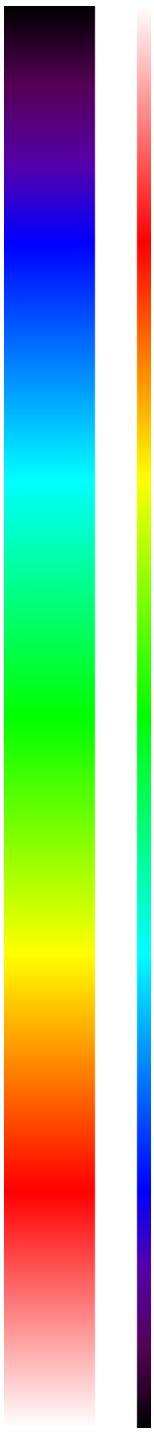

Figure 4.3: The distribution of pressure in a two-dimensional channel. Black corresponds to 0 and white corresponds to $120\rho U^2$.

### 4.1.3 Crank–Nicholson solver

The viscous term is treated with unconditional stability at the expense of using a Crank–Nicholson method. The nonlinearity associated with the advective term in the momentum equation is treated explicitly on the right-hand side. The body force term is evaluated at each cell centroid by solving (2.26) and (2.27). Since (2.26) and (2.27) are independent of time, they only need to be solved once; the resulting body force is then stored for later use. Figs. 4.4 and 4.5 show that the distribution of the external potential and the potential due to the charges at walls. The value of $\psi$ is characterized by the non-dimensional parameter $\kappa$ which is defined by

$$\kappa = \frac{h}{\lambda_D}.$$

Since $\kappa$ is so large (because of the small Debye thickness), most of the effect of the body force is concentrated near the walls. From Fig. 4.4, we see that $\varphi$ does not depend on $y$ and $\varphi$ varies linearly with $x$. From Figs. 4.4 and 4.5, it is clear that the intensity of the body force is higher near the wall. Inverting a large sparse matrix, by means of a traditional iterative technique, is computationally expensive (Press *et al.* 1997). We have developed a C$^{++}$ Crank–Nicholson solver around a core recursive multigrid routine. The Crank–Nicholson solver is based on an efficient multigrid solver that solves the Helmholtz equation

$$\nabla^2 u + \lambda u = f,$$

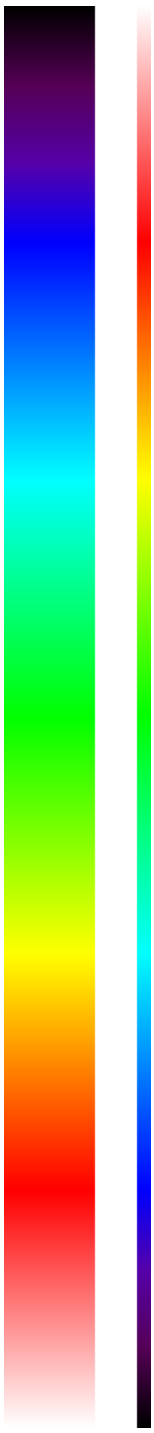

Figure 4.4: External potential field $\varphi$. Black corresponds to 0 and white corresponds to $\Phi_H$.

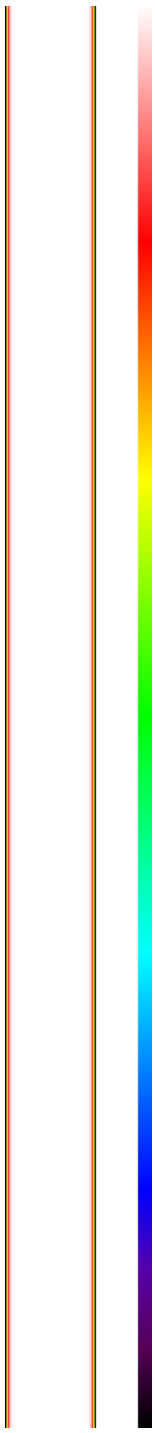

Figure 4.5: Potential $\psi$ due to the space charge. Black corresponds to $-\zeta$ and white corresponds to 0.

where $\lambda$ is a constant and $f$ is the source function. A red-black ordered Gauss–Seidel smoother is used to reduce the non-smooth component of the error in the fine grid. The divergence-free velocity computed in the previous time step is used as an initial guess. It is found that the Crank–Nicholson solver converges in about 10 iterations.

The $x$ component of the velocity field is shown in Fig. 4.6 and 4.7. Fig. 4.6 shows an early stage of the velocity field and Fig. 4.7 shows the fully developed velocity field. This velocity field is dominated by electro-osmosis, with little effect from the pressure drop. We see that the velocity is higher near the walls than in the center of the channel. In a real experiment, reduction of the effect of pressure is desirable. Since a sample is injected from the input reservoir to the output reservoir, a pressure drop may develop if the surface levels of liquid in each of the reservoirs are not maintained at the same height. The velocity field associated with pure electro-osmotic flow is shown in Fig. 4.8 and the background pressure driven flow is presented in Fig. 4.9.

## 4.2 Numerical simulation of electro-osmotic flow

The numerical code developed throughout this study has been tested to simulate passive advection by electro-osmotic flow. A wide variety of experimental results as well as analytical results of arbitrarily simplified models do exist in this case. Therefore, it is much easier to analyze the qualitative behavior of the numerical results for such a problem. We compare the flow characteristics computed by the

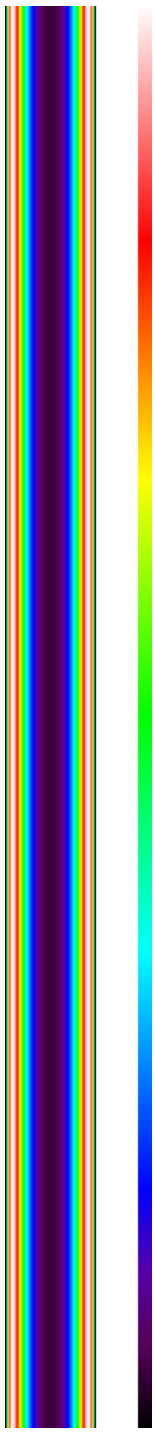

Figure 4.6: Early development of the $x$ (streamwise) component of the velocity field due to a pressure drop and a potential drop (at $t = 0.015h/U$). Black corresponds to 0 and white corresponds to $5.1U$.

Figure 4.7: Fully developed $x$ (streamwise) component of the velocity field due to a pressure drop and a potential drop. Black corresponds to 0 and white corresponds to $4.7U$.

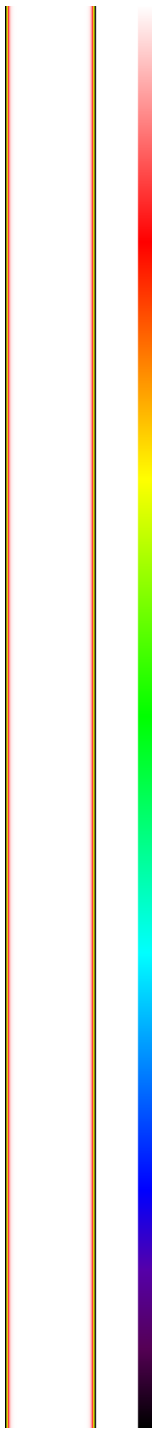

Figure 4.8: Fully developed $x$ (streamwise) component of the velocity due to a pure electro-osmotic velocity field. Black corresponds to 0 and white corresponds to $5.1U$.

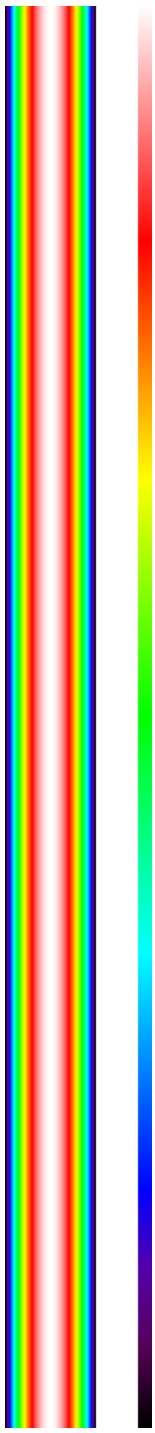

Figure 4.9: Background pressure-driven velocity field $v_x$. Black corresponds to 0 and white corresponds to $0.038U$.

numerical code with the analytical and experimental results. The numerical results are found to be in qualitative agreement with known theoretical and experimental behaviour. The results of numerical experiments are summarized in the following subsections.

### 4.2.1 General characteristics of Poiseuille and electro-osmotic flow

Many theoretical and experimental studies have been done to explain the fundamental characteristics of pressure-driven and electro-osmotic flow (Bowen *et al.* 1976; Rice & Whitehead 1965; Burgreen & Nakache 1964). Fig. 4.10 and 4.11 show the velocity profile for a Poiseuille flow and an electro-osmotic flow. The velocity has been scaled by the average velocity of a charged species observed in a typical experiment in the laboratory (Crabtree *et al.* 2000). A pressure-driven flow, generally termed Poiseuille flow, is generated by a pressure drop along the length of a channel. It has a parabolic profile. Electro-osmotic flow is generated by the Debye layer at the walls (Moyer & Gorin 1990). Having a flat velocity profile, it enhances the separation resolution of electrophoresis (Crabtree *et al.* 2000). The velocity field is independent of $x$ coordinate. The numerical velocity field is shown in Fig. 4.8 and 4.9.

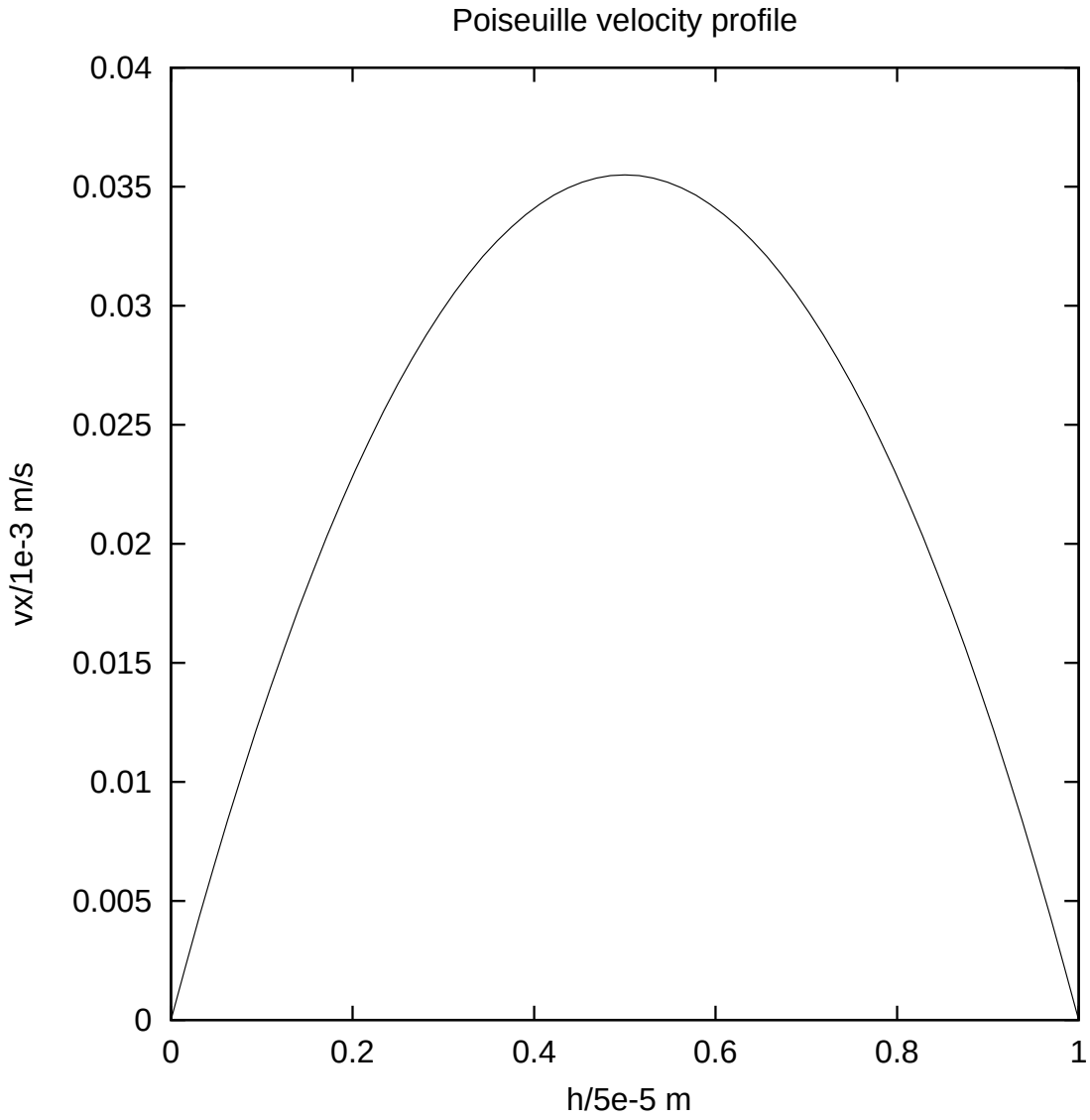


Figure 4.10: Computed pressure-driven velocity profile.

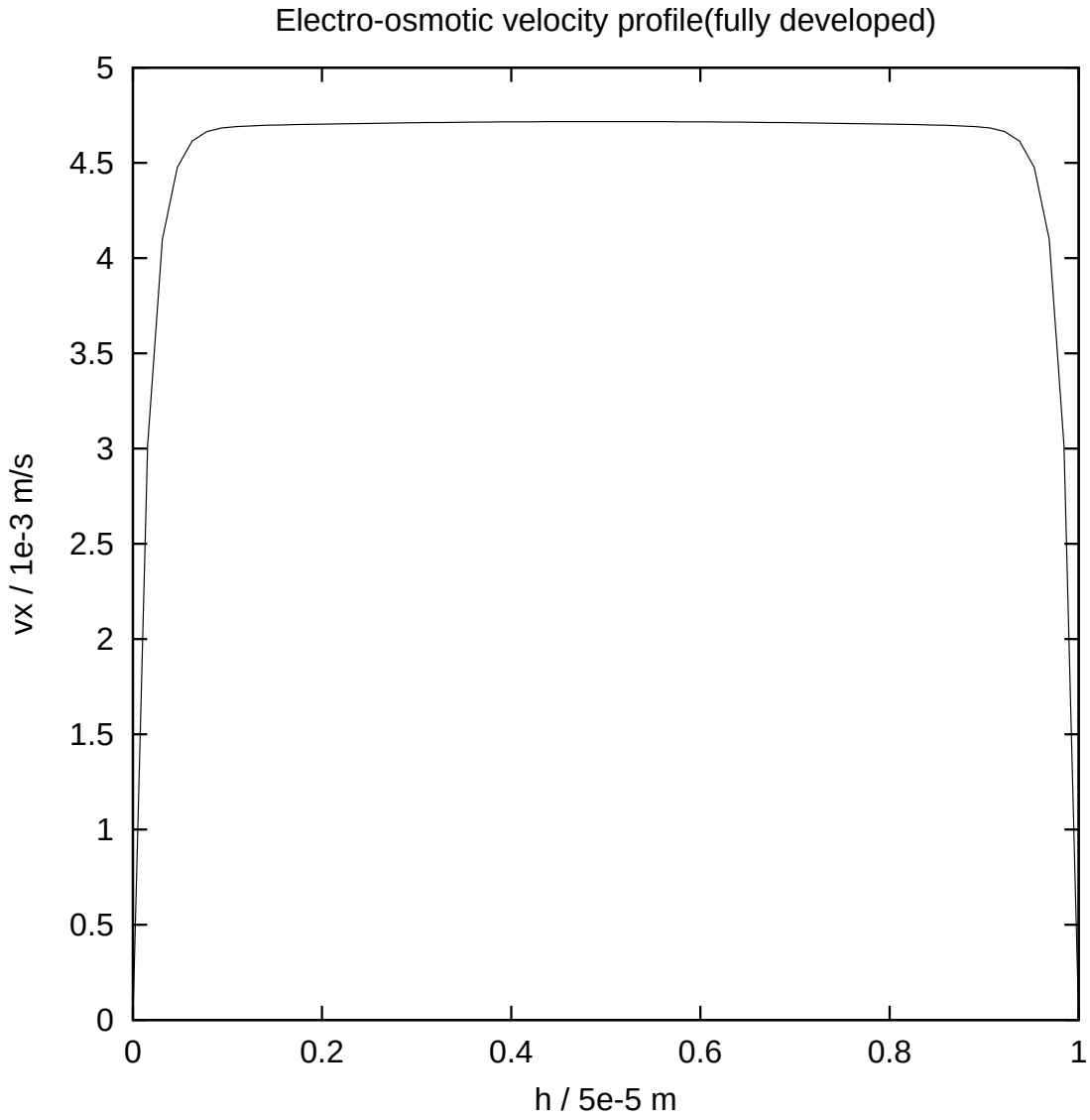


Figure 4.11: Simulated electro-osmotic velocity profile.

### 4.2.2 Electrokinetic effect on the velocity profile

In this section we study the electrokinetic effect in a very fine capillary channel of rectangular cross-section, in the presence of an applied pressure drop and potential drop. The Debye layer thickness $\lambda_D$ is small compared to the width $h$ of the channel. The ratio $\kappa = \dfrac{h}{\lambda_D}$ plays an important role in electrokinetic flow in a narrow capillary. The thickness of the Debye layer depends on the bulk ionic concentration of the liquid inside the capillary. A decrease of bulk concentration will increase the Debye thickness and decrease $\kappa$. Since the Debye layer causes electro-osmotic flow, a change in the non-dimensional parameter $\kappa$ will affect the electro-osmotic velocity profile. This effect was studied theoretically by Rice & Whitehead (1965) using a one-dimensional mathematical model. We present in Fig. 4.12 the electro-osmotic velocity profile for different values of effective ion density $n$ for a two-dimensional channel. For large values of $n$ (and hence $\kappa$) we see that the velocity has a flat profile except for a narrow region near the wall. This is the expected electro-osmotic velocity profile. As $n$ becomes smaller, divergence from electro-osmotic flow becomes noticeable. For low values of $n$, the velocity profile takes on a parabolic form, due to the overlapping of the Debye layer with the entire cross-section. When the Debye thickness is comparable with the characteristic length scale $h$, $\psi$ becomes important far away from the walls.

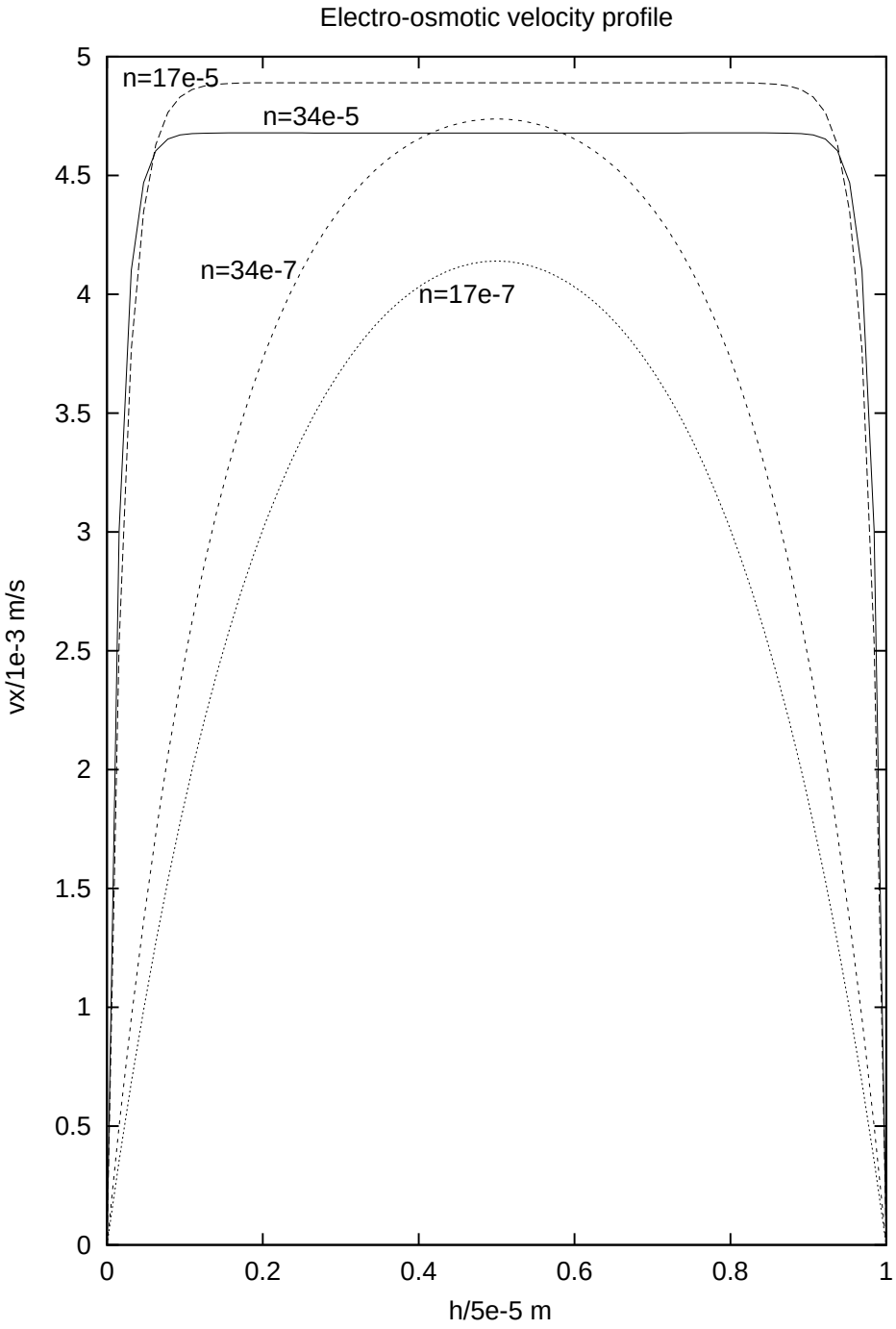


Figure 4.12: Electro-osmotic velocity profile at various values of $n$ in mol/m$^3$.

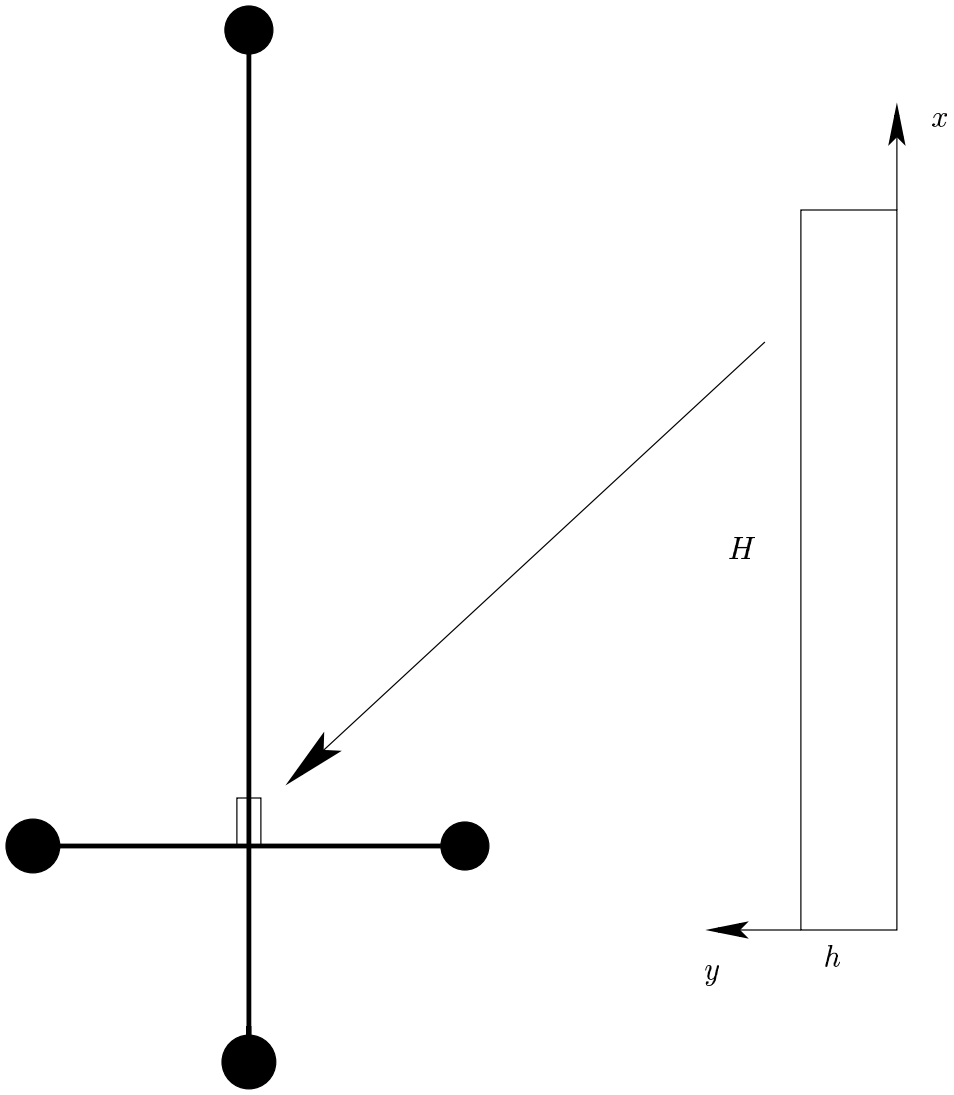


Figure 4.13: A cross-channel microfluidic device and the computational domain.

### 4.2.3 Poiseuille flow vs. electro-osmotic flow

In many experiments in the laboratory, a cross-channel microfluidic device is used as shown in Fig. 4.13. Initially the height of the liquid is kept the same in all reservoirs. When the sample solution begins to move towards the separation junction, the liquid height of sample input and sample output reservoirs changes. Thus a pressure-driven flow is imposed in the direction opposite to that of electro-osmotic flow. It is necessary to arrange the sample species in such a way that it can move in response to the electric field (Patankar & Hu 1998). Electro-osmotic flow does this very efficiently. The presence of a pressure-driven flow in the opposite direction affects the role of the electro-osmotic flow. In Figs. 4.10 and 4.11 we compare pressure-driven and electro-osmotic velocity profiles, where both velocities are in the same direction. In Fig. 4.14, we illustrate passive advection for a velocity field that is a combination of Poiseuille and electro-osmotic flow.

## 4.3 Passive advection of the concentration field

Diffusion of the injected sample is typically very small in the case of electrophoresis (Patankar & Hu 1998). For the experimental parameters, the dimensionless diffusion coefficient $\nu_c = 2 \times 10^{-4}$ is so small that diffusion is much weaker than the electrophoretic motion. This is illustrated in Fig. 4.19. The weak pressure gradient

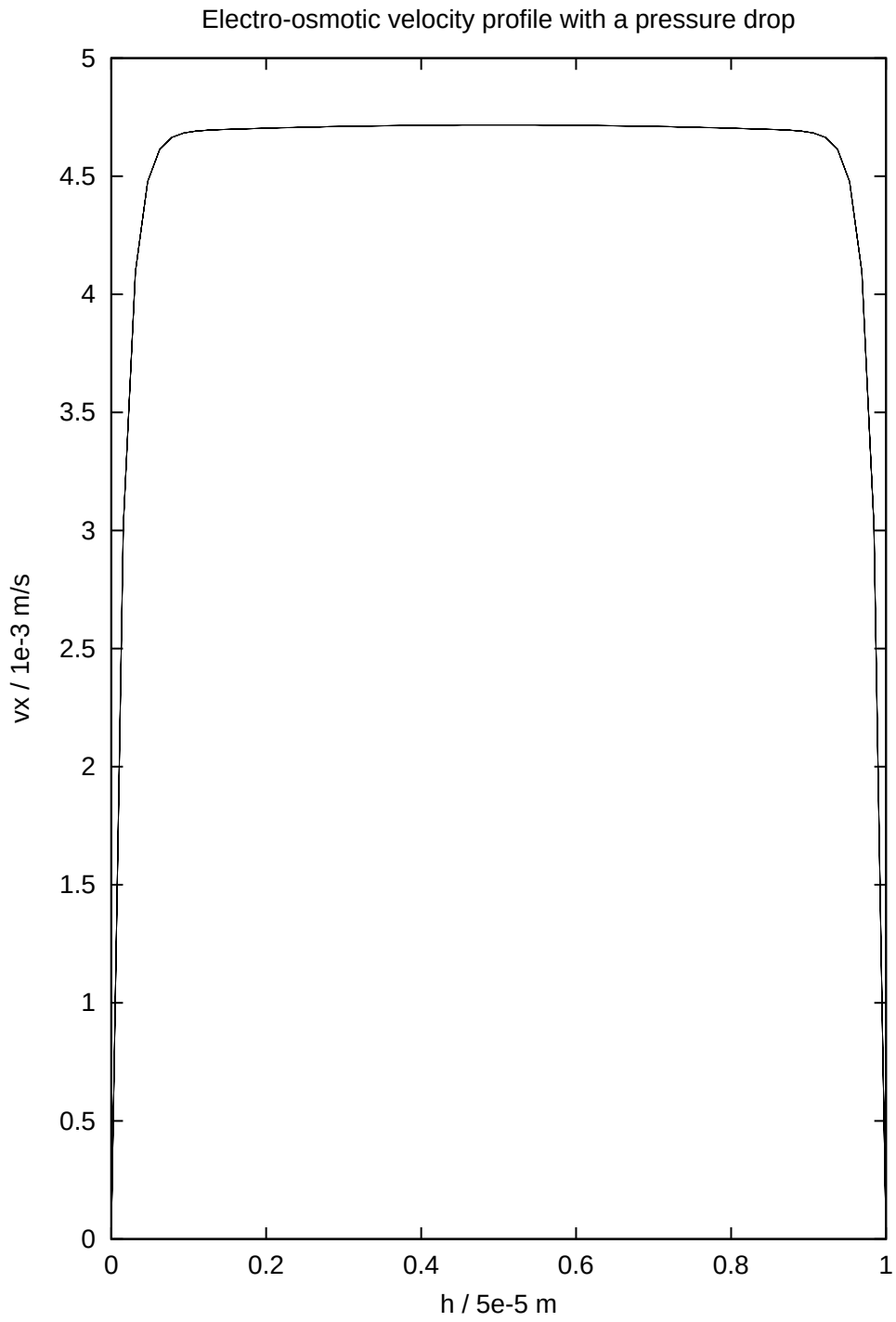


Figure 4.14: Velocity profile due to a pressure drop and a potential drop.

produces a small velocity and a very long time is required to transport a sample from the input to output reservoirs. We observe significant diffusion even though $\nu_c$ is so small (see Fig. 4.25).

### 4.3.1 Passive advection

We present here the advection of a passive scalar by a prescribed velocity field. In this two-dimensional simulation, we solved a pure advection equation with the parcel advection algorithm, where the non-dimensional velocity field is given by

$$v_x = \frac{1}{2} y(1-y)\,, \quad v_y = 0. \tag{4.1}$$

We also tried several other flows including flow with rotation and shear. Passive advection of $C$ by the parabolic velocity field (4.1) is shown in Fig. 4.15. Parcel advection can predict passive advection more accurately than an Eulerian (or even semi-Lagrangian) code. The parcels are advected in Lagrangian coordinates using an area-weighted average velocity from the cells. This does not require the addition of any artificial diffusion either explicitly or implicitly. Next, parcel advection was applied to the passive advection model described in Sec. 2.2, where the velocity field is obtained by numerical solution of the incompressible Navier–Stokes equation. The initial distribution of $C$ is shown in Fig. 4.16. In Figs. 4.18 and 4.19 we compare the advection of $C$ by a first-order upwind method written in flux-conservative form and by the parcel advection method, respectively. The stability of the upwind scheme

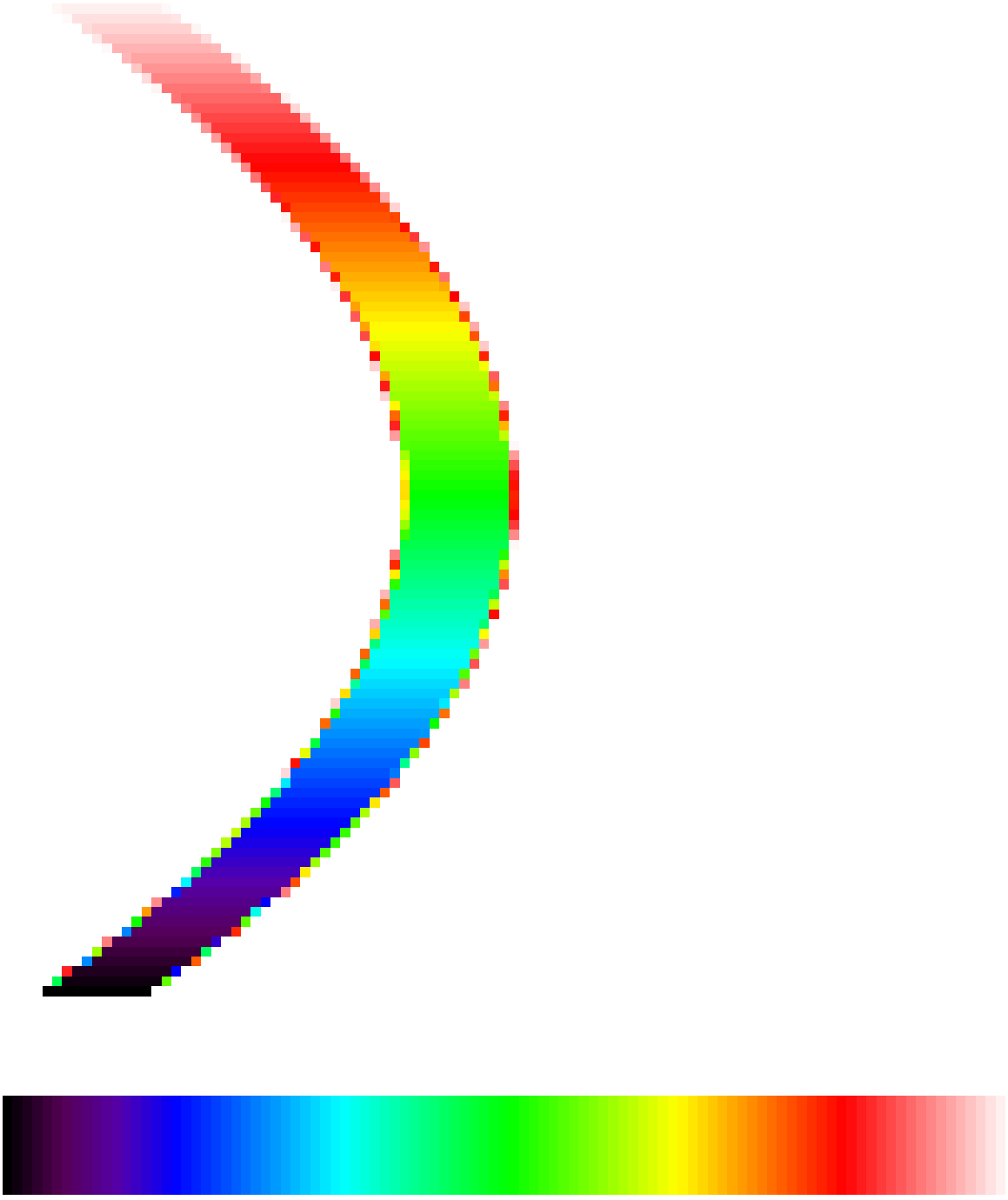

Figure 4.15: Concentration field predicted by the parcel advection algorithm after a few time steps, where the velocity field is explicitly known. The large pixels illustrate the coarse graining of output quantities in the parcel advection scheme.

Figure 4.16: Initial distribution of the concentration. Black corresponds to 0 and white corresponds to 1.

has been achieved at the expense of an artificial diffusion, which is not present in the parcel advection results. These results establish that the Lagrangian parcel advection method is more faithful to the underlying physics than the Eulerian upwind scheme.

### 4.3.2 The concentration distribution

Numerical experiments have been performed to understand the concentration distribution in a passive advection problem. A passively traveling rectangular-shaped pulse in $C$ has been simulated with the parcel advection algorithm. The distribution of $C$ is plotted in Fig. 4.17 at the beginning of the simulation.

We perform four different simulations: (a) flow driven by a potential drop and a pressure drop; (b) flow driven by only a potential drop; (c) flow with the pressure term explicitly removed from the momentum equation; (d) flow driven by only a pressure drop. Case (c) is rather unphysical. However, it is done to emphasize the necessity of retaining the pressure term even when the pressure drop is very small. Figs. 4.19, 4.20, and 4.21 show the concentration fields in these three simulations. In Figs. 4.23 and 4.24, we show the concentration distribution sampled at $x = 15$, $y = 0.5$. The effect of pressure on electro-osmotic flow can be understood if we compare Fig. 4.19 with Fig. 4.20. The curved pulse of $C$ in Fig. 4.19 is due to the background pressure-driven flow. The effect of the pressure drop is very small compared with that of the external potential drop; that is, the parabolic effect in

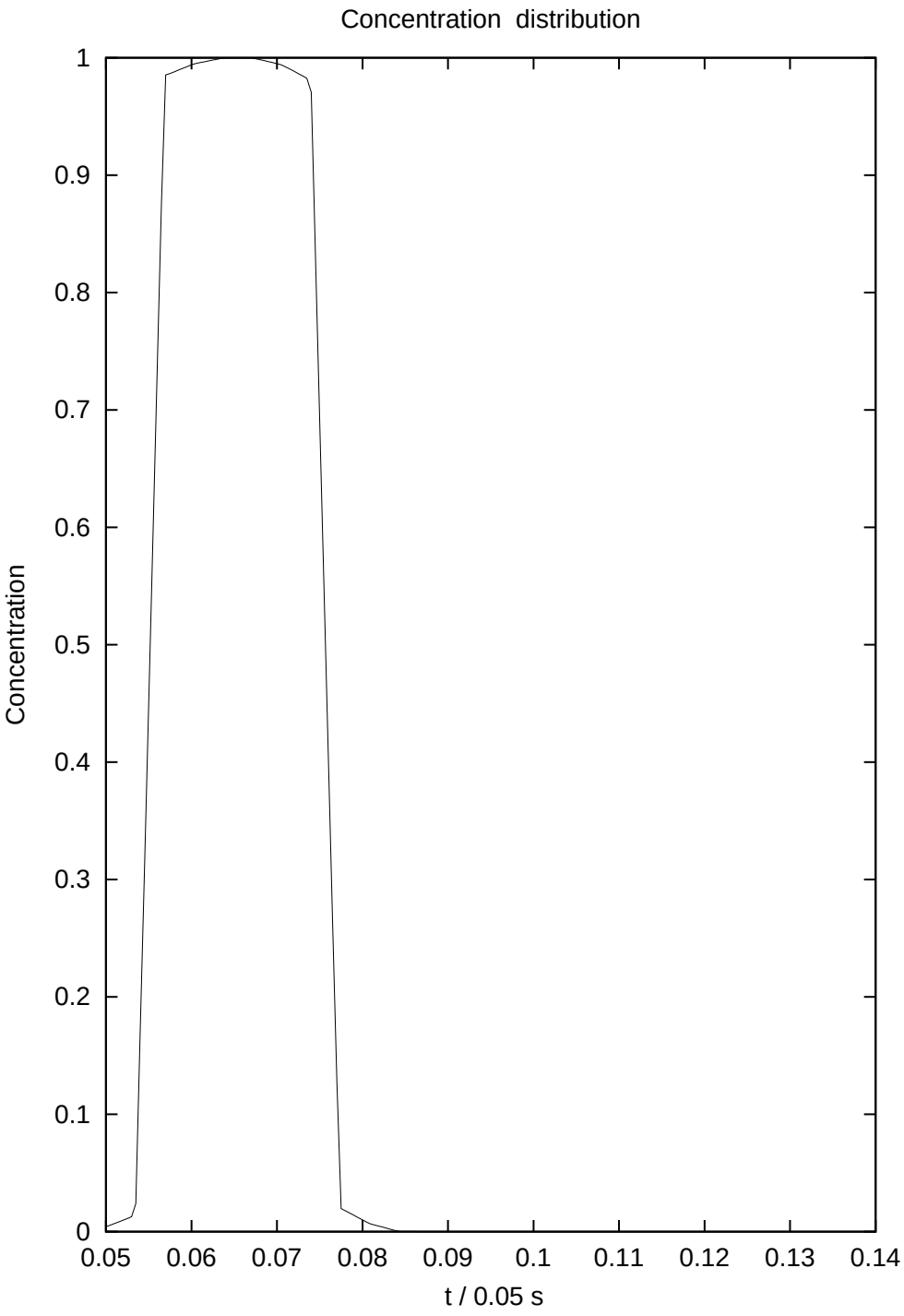


Figure 4.17: Early distribution of $C$.

Fig. 4.19 is weaker than the osmotic effect. The effect of only a pressure drop but without potential drop on the concentration field is shown in Fig. 4.22. We observe that the parcel advection code can follow a passively traveling pulse of a certain scalar quantity without introducing any numerical diffusion.

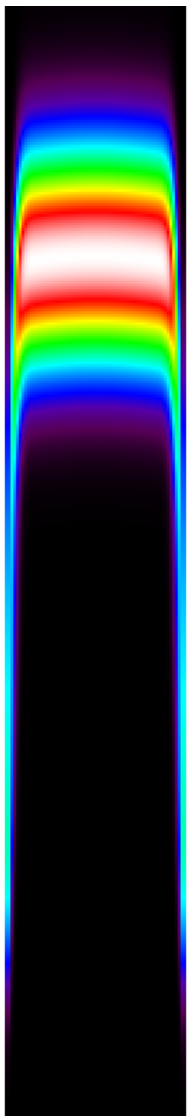

Figure 4.18: Passive advection of the concentration field by a first-order upwind method. Black corresponds to 0 and white corresponds to 1.

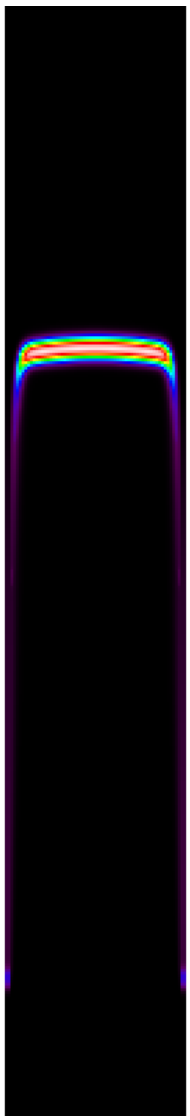

Figure 4.19: The concentration field advected by an electro-osmotic flow and a pressure-driven flow. Black corresponds to 0 and white corresponds to 1.

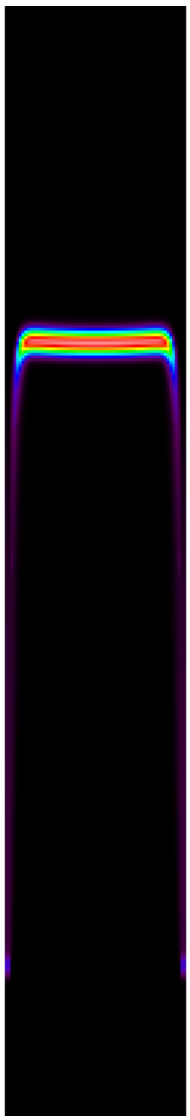

Figure 4.20: The concentration field advected by a pure electro-osmotic flow. Black corresponds to 0 and white corresponds to 1.

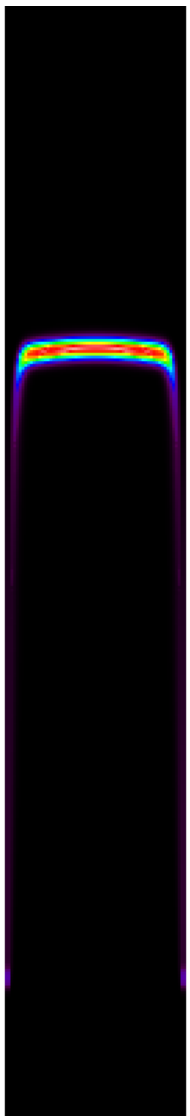

Figure 4.21: The concentration field in simulation (c) advected by a flow, where the pressure effect is neglected explicitly. The resulting violation of incompressibility produces spurious results. Black corresponds to 0 and white corresponds to 1.2.

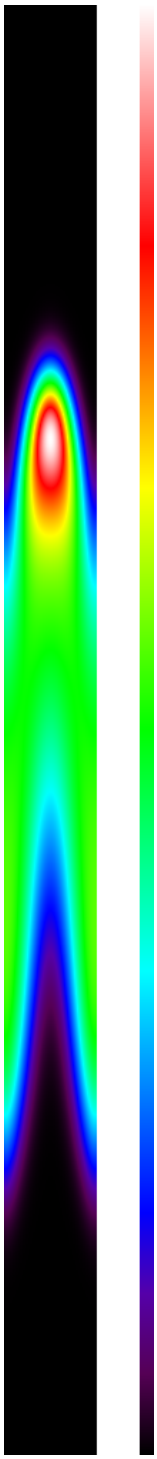

Figure 4.22: The concentration field $C$ due to pressure-driven flow in the absence of an electric field. Black corresponds to 0 and white corresponds to $0.028U$.

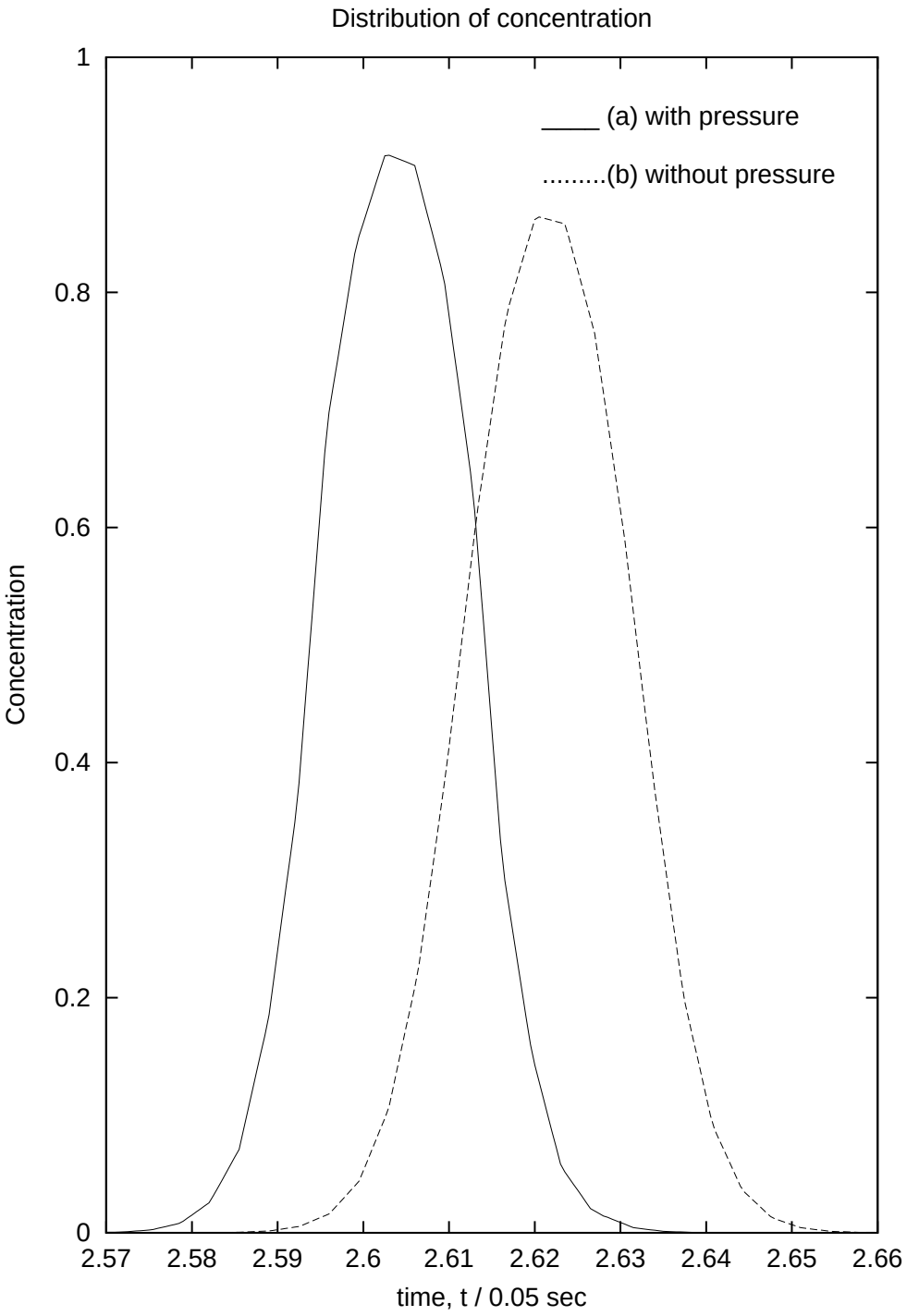


Figure 4.23: Distribution of $C$ along the center line in simulation (a) and (b).

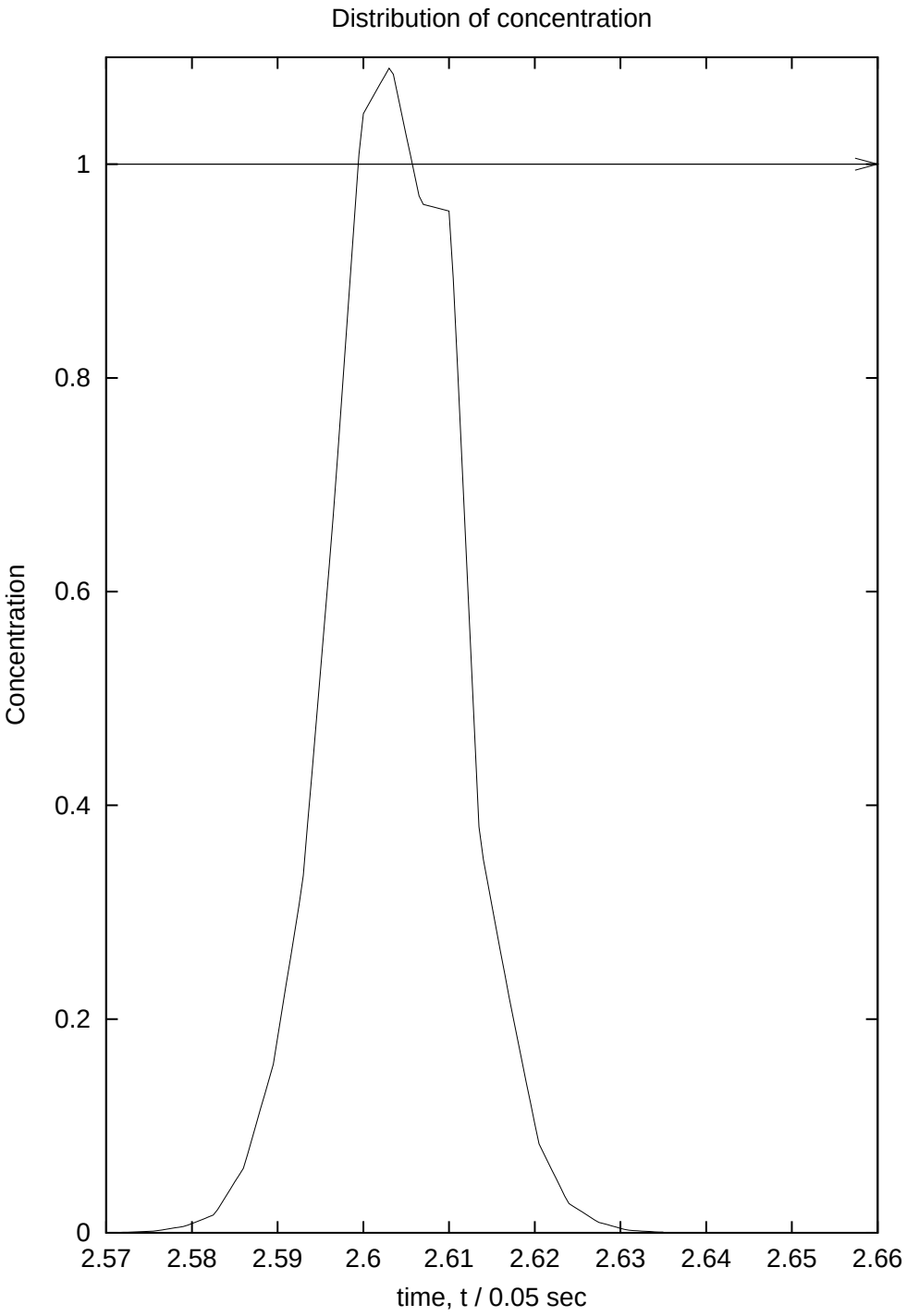


Figure 4.24: Distribution of $C$ in simulation (c).

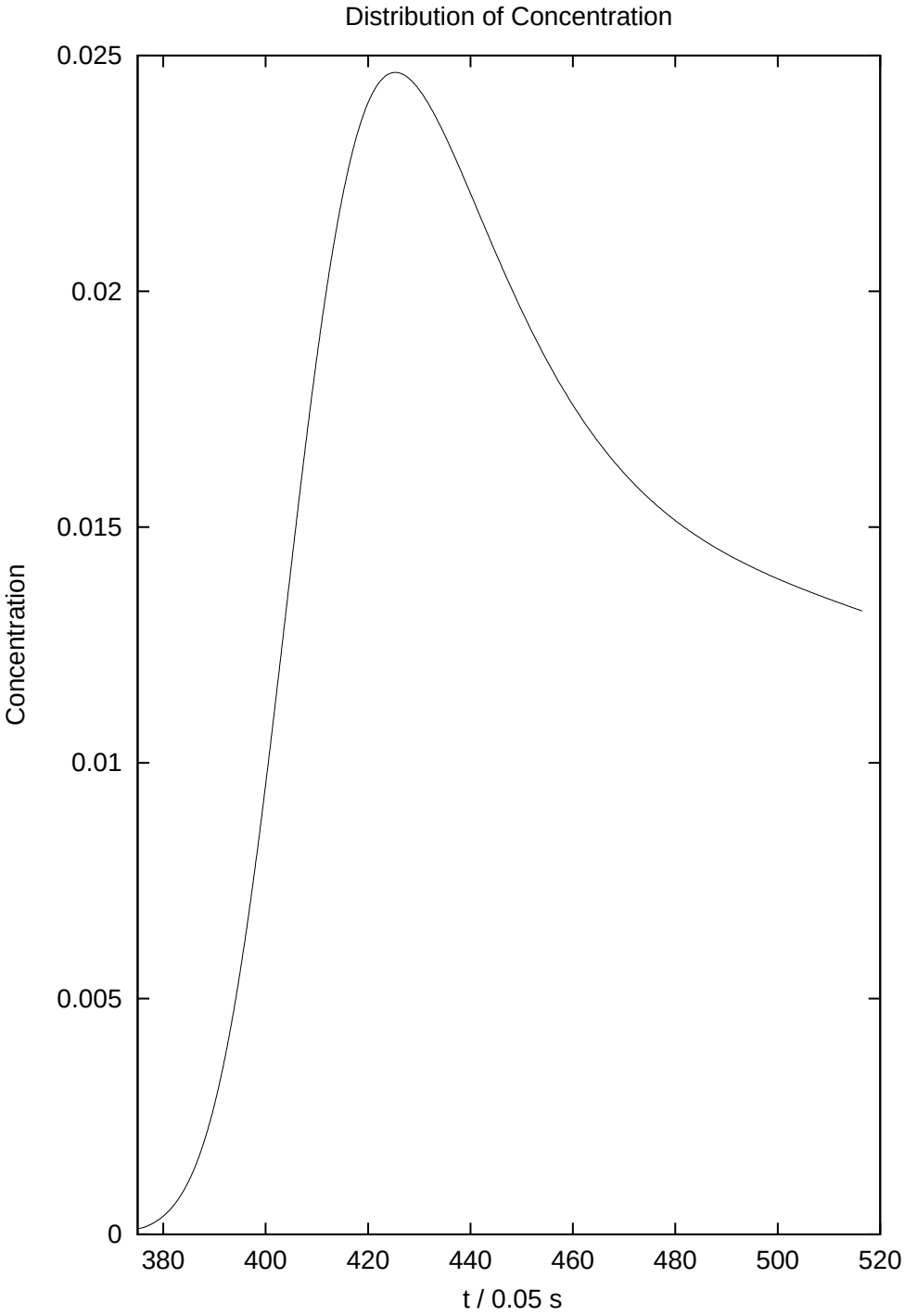


Figure 4.25: Concentration distribution along the center line for simulation (d), with the electric field absent.

# Chapter 5

# CONCLUSION

## 5.1 Discussion

The main contribution of this work was the development of a new numerical method, parcel advection, to simulate passive advection by electro-osmotic flow. A semi-implicit finite difference method was used to solve the incompressible Navier-Stokes equation, which prescribes the advective velocity field everywhere in the domain. The fluid is modeled as a collection of parcels, each of which has a mean velocity, a mean concentration and a mean position. We used an Eulerian grid to solve the momentum equation. The fluid body force is evaluated by solving a Laplace equation and a Helmholtz equation. The pressure is calculated at each cell centroid by solving a Poisson equation. We used a different stencil to discretize the Laplacian of the

pressure Poisson equation. This differencing is central in space and still affords second-order accuracy. However, the usual compact stencil for a Laplacian differencing does not provide a divergence-free velocity. Therefore, it was essential to deviate from the traditional compact formula to ensure a divergence-free velocity in each numerical computation.

A $C^{++}$ multigrid Crank–Nicholson solver has been developed for handling the viscous terms, which for the velocity equations are dominant. This solver converges rapidly, independent of the number of grid points. Once the velocity field is updated *via* the Navier–Stokes equation, the concentration equation is solved in Lagrangian coordinates using the parcel advection algorithm. At each time step, a parcel is assigned new velocities according to an area-weighted average of the fluid velocities in the cells it overlaps. In a similar manner parcels distribute their concentration to the cells they overlap. The parcel advection algorithm was found to work very nicely if the velocity field is already known. Although the Eulerian upwind method can provide a stable numerical scheme for passive advection, it introduces too much numerical diffusion for the problem at hand. Moreover, in the case where a concentration field is advected, an upwind scheme does not guarantee that the evolved scalar remains everywhere non-negative.

Parcel advection differs significantly from the particle-in-cell method developed in Los Alamos in 1955 and later variations such as the cloud-in-cell methods. Parcel advection uses distributed square parcels of grid size having nonuniform scalar

values, instead of many uniform particles per cell. The fluid is modeled as being fundamentally composed of parcels, not particles, so the algorithm can readily handle nonuniform particle densities without losing resolution. Like certain refinements of the original particle-in-cell method, parcel advection uses area weighting instead of the nearest grid-point method in the calculation of grid (output) quantities, thereby reducing statistical noise. Our parcel advection algorithm treats diffusion using a traditional Eulerian scheme *via* operator splitting), rather than introducing a heuristic collision operator, as is done in many particle-in-cell codes.

One alternate to the upwind method is the flux-corrected transport algorithm of Boris & Book (1964). The ideas underlying this Eulerian method are based on Lagrangian considerations. Although this method can ensure positivity of the transported quantity and has been tested for several applications (Boris & Book 1976), the enormous amount of numerical diffusion forced the algorithm to introduce an anti-diffusion stage (Boris & Book 1964). The anti-diffusion stage of this algorithm is somehow problem-dependent and must be adjusted according to the particular problem (Boris & Book 1964), although it has been shown to work for a square-wave problem much better than the upwinding method did.

The numerical experiments were conducted to explain transport phenomenon such as electro-osmosis, passive advection, and diffusion. Although the simulations were two-dimensional, this is thought to be a good approximation to describe passive transport by electro-osmotic flow (Patankar & Hu 1998). Furthermore, the numerical

code has been designed so that it can be readily generalized to three dimensions. Our simulations emphasize that diffusion cannot be neglected if the duration of advection is comparable with the diffusion time scale. Pressure effects could in principle halt, retard or reverse electro-osmotic pumping. The flat velocity profile of electro-osmotic flow show that such a pumping allows the sample species to be arranged so that each species can be ready to move in response to the electric field. In the case of a flow driven by a small pressure gradient, diffusion was noticeable because the duration of the advection was comparable to the diffusion time scale.

We notice that a number of numerical schemes do exist to solve an advection equation. Numerical solutions of an advection equation by various schemes can be found in a number of references (Holt 1984; LeVeque 1990; Tannehill *et al.* 1997). However, if there is a sharp gradient in the solution, the Eulerian numerical methods have difficulties (Woodward & Colella 1984; LeVeque 1990). We found that our parcel advection algorithm predicted the solution of an advection equation very well, even when a sharp gradient exists in the solution.

## 5.2 Future work

Throughout this study, the parcel advection algorithm has been tested and applied to study two-dimensional passive advection in a rectangular geometry. The results were found to be surprisingly good. This algorithm can be readily extended to three

dimensions. Until now, parcel distortion has been neglected, but should be taken into account. Once parcel stretching and rotation are considered, this algorithm can be applied successfully to flows with shear. A semi-implicit numerical scheme has been used to prescribe the velocity field. Applying the parcel advection scheme itself to update the parcel velocities each time step has been left as a future task. It is also necessary to generalize our simulations to complex geometries since the devices used in real-life experiments sometimes have shapes more complicated than a rectangular channel. The parcel advection algorithm can easily be implemented in any geometry.

An alternate way of successfully representing complex geometry in a numerical grid is the finite element method. Since the Debye thickness, which plays a major role in producing electro-osmotic flow, is very small compared with the cell size, it would be better to use a very fine grid near the wall. To address this problem and corner effects in complicated geometries successfully, a finite element simulation of electrophoretic transport would be a significant contribution to this field. It has been observed that an application of the multigrid method to finite element discretization is not difficult.

# Appendix A

# Debye-Hückel approximation

The space charge density can be written as:

$$\rho_e = n_i e - n_e e,$$

where

$n_i e$ is the ionic charge density,

$n_e e$ is the electronic charge density.

The potential $\psi$ satisfies the Poisson equation

$$\nabla^2 \psi = -\frac{\rho_e}{\epsilon},$$

which can be written as

$$\epsilon \nabla^2 \psi = -e(n_i - n_e). \tag{A.1}$$

The distribution of electrons in space is assumed to be a Gibbs distribution. This implies that

$$n_e = n_e^{(0)} \exp\left(\frac{e\psi}{KT}\right),$$

where

$K$ is the Boltzmann constant

and

$T$ is the absolute temperature.

This is known as the Boltzmann relation.

We know that the Boltzmann constant is $1.38 \times 10^{-23}\mathrm{J/K}$ and $e$ is $1.6 \times 10^{-19}\mathrm{C}$. Taking a typical value for the potential, $\psi = 0.1\,\mathrm{V}$, it is reasonable to assume that $|\frac{e\psi}{KT}| \ll 1$. Therefore, we can write the electron distribution as:

$$n_e \approx n_e^{(0)} \left(1 + \frac{e\psi}{KT}\right).$$

Hence, (A.1) can be written as

$$\begin{aligned}
\epsilon\nabla^2\psi &= -e\,(n_i - n_e) \\
&= -e\,n_e^{(0)}(1 - 1 - \frac{e\psi}{KT}) \\
&= \frac{e^2 n_e^{(0)}\psi}{KT}. \\
\Rightarrow \quad \nabla^2\psi &= \frac{\psi}{\lambda_D^2},
\end{aligned}$$

where

$$\lambda_D^2 = \frac{KT\epsilon}{e^2 n_e^{(0)}} \quad \text{is the squared Debye length.}$$

# Appendix B

# Theoretical analysis

## B.1 Conservation laws

Here we review the theories of Obukhov, Corrsin, and Batchelor to predict the inertial-range wavenumber behaviour of the spectrum $\mathcal{C}(k)$ of a scalar field that is advected by high-Reynolds number turbulence. The spectrum of a scalar field depends on the Schmidt number that is defined by

$$S_c = \frac{\nu}{D}. \tag{B.1}$$

The origin of these theories is the work of Kolmogorov in 1941, where the famous $k^{-5/3}$ scaling law of the inertial range energy spectrum of homogeneous isotropic three-dimensional turbulence was proposed (Kolmogorov 1941). Since then, numerical and experimental investigations have been performed to verify the scaling law, which

was originally derived based on dimensional arguments. The original Kolmogorov spectrum was extended to the two-dimensional case by Kraichnan (1971). Recently, a correction to the original Kolmogorov energy spectrum was derived by Bowman (1996). Corrsin (1951) argued that the Kolmogorov hypothesis can be extended to the spectrum of a scalar (mean-squared concentration).

We start our discussion by describing the four quadratic integral invariants in $x$ space. When the flow is inviscid, the diffusion of the scalar field is neglected, and the forcing is absent, the energy $E$ (mean-squared velocity) and mean-squared concentration $\mathcal{C}$ are invariant both in two- and three-dimensional turbulence. In two-dimensional turbulence, two additional quantities are conserved by the inviscid dynamics, the enstrophy $Z$ (mean-squared vorticity) and cross-correlation of vorticity and concentration $I$. The four quantities $E$, $C$, $Z$, and $I$ are related to the fields $\boldsymbol{v}$ and $C$ by

$$E = \frac{1}{2}\int v^2 d\mathbf{x},$$
$$\mathcal{C} = \frac{1}{2}\int C^2 d\mathbf{x},$$
$$Z = \frac{1}{2}\int \omega^2 d\mathbf{x},$$
$$I = \frac{1}{2}\int C\omega d\mathbf{x},$$

where the scalar $\omega$ is the magnitude of the vorticity

$$\boldsymbol{\omega} = \boldsymbol{\nabla} \times \boldsymbol{v}.$$

Energy is conserved in two and three dimension since in the absence of dissipation

and forcing, (2.23) leads to

$$\frac{\partial \boldsymbol{v}}{\partial t} = -\boldsymbol{v} \cdot \boldsymbol{\nabla} \boldsymbol{v} - \boldsymbol{\nabla} P.$$

Then

$$\begin{aligned}
\frac{\partial E}{\partial t} &= -\int \boldsymbol{v} \cdot \frac{\partial \boldsymbol{v}}{\partial t} d\boldsymbol{x} \\
&= -\int \boldsymbol{v} \cdot \boldsymbol{\nabla} \left( \frac{v^2}{2} + P \right) d\boldsymbol{x} \\
&= -\int \boldsymbol{\nabla} \cdot \left[ \left( \frac{v^2}{2} + P \right) \boldsymbol{v} \right] d\boldsymbol{x} + \int \left( \frac{v^2}{2} + P \right) (\boldsymbol{\nabla} \cdot \boldsymbol{v}) \, d\boldsymbol{x} \\
&= 0.
\end{aligned}$$

The second integral vanishes due to the incompressibility condition (2.15) and the first integral vanishes if the flux $(v^2/2 + P)\,\boldsymbol{v}$ vanishes on the boundary or if periodic boundary conditions are used.

The mean-squared concentration $\mathcal{C}$ is conserved in two and three dimensions when the diffusion coefficient $D = 0$ since (2.14) then leads to

$$\begin{aligned}
\frac{\partial C}{\partial t} &= -\boldsymbol{v} \cdot \boldsymbol{\nabla} C + \mu \boldsymbol{\nabla} \varphi \cdot \boldsymbol{\nabla} C \\
&= -\boldsymbol{\nabla} \cdot (\boldsymbol{v} C - \mu \boldsymbol{\nabla} \varphi C) + C \, (\boldsymbol{\nabla} \cdot \boldsymbol{v}) - \mu C \nabla^2 \varphi \\
&= -\boldsymbol{\nabla} \cdot (\boldsymbol{v} C - \mu \boldsymbol{\nabla} \varphi C) \, .
\end{aligned}$$

Therefore,

$$\begin{aligned}
\frac{\partial \mathcal{C}}{\partial t} &= \int C \frac{\partial C}{\partial t} d\boldsymbol{x} \\
&= -\int C \boldsymbol{\nabla} \cdot (\boldsymbol{v} C - \mu \boldsymbol{\nabla} \varphi C) \, d\boldsymbol{x}
\end{aligned}$$

$$= -\int \boldsymbol{\nabla} \cdot \left( \boldsymbol{v} \frac{C^2}{2} - \mu \boldsymbol{\nabla} \varphi \frac{C^2}{2} \right) d\boldsymbol{x}$$
$$= 0.$$

In two dimensions we have the two additional quadratic invariants $Z$ and $I$. If the velocity field is two dimensional, there is no dependence in the $z$ direction, it follows that $\boldsymbol{\omega} = \boldsymbol{\nabla} \times \boldsymbol{v} = \omega \hat{z}$. Taking the curl of (2.12), when the flow is inviscid and forcing is absent, we get the vorticity equation for 2-D flow:

$$\frac{\partial \omega}{\partial t} + \boldsymbol{v} \cdot \nabla \omega = 0.$$

Thus,

$$\frac{\partial Z}{\partial t} = \int \omega \frac{\partial \omega}{\partial t} d\boldsymbol{x}$$
$$= -\int \boldsymbol{v} \cdot \nabla \left( \frac{\omega^2}{2} \right) d\boldsymbol{x}$$
$$= 0.$$

Again,

$$\frac{\partial I}{\partial t} = \frac{1}{2} \int C \frac{\partial \omega}{\partial t} \, d\boldsymbol{x} + \frac{1}{2} \int \omega \frac{\partial C}{\partial t} \, d\boldsymbol{x}$$
$$= -\frac{1}{2} \int C \boldsymbol{v} \cdot \boldsymbol{\nabla} \omega \, d\boldsymbol{x} - \frac{1}{2} \int \omega \boldsymbol{v} \cdot \boldsymbol{\nabla} C \, d\boldsymbol{x} + \frac{1}{2} \int \omega \mu \boldsymbol{\nabla} \varphi \cdot \boldsymbol{\nabla} C \, d\boldsymbol{x}$$
$$= -\frac{1}{2} \int \boldsymbol{\nabla} \cdot \left( \boldsymbol{v} C \omega - \mu \boldsymbol{\nabla} \varphi C \omega \right) \, d\boldsymbol{x} - \frac{1}{2} \int \mu C \boldsymbol{\nabla} \varphi \cdot \boldsymbol{\nabla} \omega \, d\boldsymbol{x}.$$

Again, the surface integrals vanish because of the boundary conditions. If $\mu = 0$ we see that $I$ is conserved. Note that mean-squared concentration $\mathcal{C}$ but not the cross-correlation $I$ is conserved in the presence of the electrophoretic term.

## B.2 Fourier analysis of the equation of motion

In this section we will give a brief description of the Fourier analysis of the equations of motion. The principal reason for using Fourier analysis is that this converts spatial differential operators into multipliers, giving us a relatively simple picture of the underlying physics. Further details of Fourier analysis is illustrated by Stuart (1961).

Any differentiable periodic function $f(\boldsymbol{x})$ with a period $2\pi$ can be decomposed into the Fourier series

$$f(\boldsymbol{x}) = \sum_{k=-\infty}^{\infty} F_{\boldsymbol{k}} e^{i\boldsymbol{k}\cdot\boldsymbol{x}},$$

where the Fourier coefficients $F_{\boldsymbol{k}}$ are given by

$$F_{\boldsymbol{k}} = \frac{1}{L}\int_{-L/2}^{L/2} f(\boldsymbol{x}) e^{-i\boldsymbol{k}\cdot\boldsymbol{x}} d\boldsymbol{x}.$$

In the limit of $L \to \infty$ we can define a Fourier transform pair

$$f(\boldsymbol{x}) = \int_{-\infty}^{\infty} F(\boldsymbol{k}) e^{i\boldsymbol{k}\cdot\boldsymbol{x}} d\boldsymbol{k},$$
$$F(\boldsymbol{k}) = \frac{1}{2\pi}\int_{-\infty}^{\infty} f(\boldsymbol{x}) e^{-i\boldsymbol{k}\cdot\boldsymbol{x}} d\boldsymbol{x}.$$

In the case of a scalar transport, we must consider fluctuations about a constant mean level of concentration. For the velocity field we may choose a system of coordinates in which the constant mean velocity is zero. We restrict our attention to homogeneous and isotropic fields. This implies that statistical quantities do not depend upon absolute position in space. We decompose instantaneous variables into a mean and a

fluctuation from the mean. We assume that constant mean velocity is zero with respect to the system of coordinates and concentration field fluctuates about a constant mean fluctuation. With this assumption, the fluctuating quantities satisfy the same equations. The equations of motion can be written using tensor notation:

$$\frac{\partial v_i}{\partial x_i} = 0, \tag{B.2}$$

$$\frac{\partial v_i}{\partial t} + \frac{\partial}{\partial x_m}(v_m v_i) = -\frac{\partial P}{\partial x_i} + \nu \nabla^2 v_i, \tag{B.3}$$

$$\frac{\partial C}{\partial t} + \frac{\partial}{\partial x_m}(v_m C) = D \nabla^2 C. \tag{B.4}$$

Note that summation over repeated indices is implied.

If we take the Fourier transform of (B.2)–(B.4), the effect will be to replace the differential operator $\partial/\partial \boldsymbol{x}_j$ by its analogous wavenumber $i\boldsymbol{k}_j$ So we can write the Fourier transform of (B.2)–(B.4) as:

$$k_i u_i(\boldsymbol{k}) = 0, \tag{B.5}$$

$$\left(\frac{\partial}{\partial t} + \nu k^2\right) u_i(\boldsymbol{k}) = -ik_i P(\boldsymbol{k}) - ik_m \int d^3\boldsymbol{p}\, u_i(\boldsymbol{k}-\boldsymbol{p}) u_m(\boldsymbol{p}), \tag{B.6}$$

$$\left(\frac{\partial}{\partial t} + Dk^2\right) C(\boldsymbol{k}) = -ik_m \int d^3\boldsymbol{p}\, u_m(\boldsymbol{p}) C(\boldsymbol{k}-\boldsymbol{p}). \tag{B.7}$$

After multiplying (B.6) by $k_i$ and summing over $i$ we get

$$P(\boldsymbol{k}) = -\frac{k_j k_m}{k^2} \int d^3\boldsymbol{p}\, u_j(\boldsymbol{k}-\boldsymbol{p}) u_m(\boldsymbol{p}),$$

where we have used the incompressibility constraint (B.5) and $i$ is replaced with $j$ for convenience.

Hence (B.6) can be written as (Leslie 1973; McComb 1996)

$$\left(\frac{\partial}{\partial t} + \nu k^2\right) u_i(\boldsymbol{k}) = M_{ijm}(\boldsymbol{k}) \int d^3\boldsymbol{p}\, u_j(\boldsymbol{k}-\boldsymbol{p}) u_m(\boldsymbol{p}), \tag{B.8}$$

where

$$M_{ijm}(\boldsymbol{k}) = i\left(\frac{k_i k_j k_m}{k^2} - k_m \delta_{ij}\right)$$

has the following properties:

$$M_{ijm}(-\boldsymbol{k}) = -M_{ijm}(\boldsymbol{k}),$$

$$M_{ijm}(\boldsymbol{k}) = -ik_m P_{ij}(\boldsymbol{k}),$$

$$P_{ij}(\boldsymbol{k}) = \delta_{ij} - \frac{k_i k_j}{k^2}.$$

Note that the energy is defined by

$$E = \frac{1}{2}\langle u_i(\boldsymbol{x}) u_i(\boldsymbol{x})\rangle = \int_0^\infty E(k)\, dk,$$

where $\langle\rangle$ denotes an ensemble average.

The mean-squared concentration is defined by

$$\mathcal{C} = \frac{1}{2}\langle C(\boldsymbol{x}) C(\boldsymbol{x})\rangle = \int_0^\infty \mathcal{C}(k)\, dk.$$

An equation for the energy spectrum $E(k)$ can derived from (B.8) as below:

$$\left(\frac{d}{dt} + 2\nu k^2\right) E(k) = T(k), \tag{B.9}$$

where the right hand side, which arises from the non-linear terms of (B.8), satisfies

$$\int_0^\infty T(k)\, dk = 0. \tag{B.10}$$

Further details of this is explained by Leslie (1973) and McComb (1996). It then follows that the nonlinear term $T(k)$ conserves energy in the inviscid limit. Let $\Pi(k)$ be the rate of energy transfer from wavenumbers lower than $k$ to wavenumbers higher than $k$ (e.g., see Bowman (1996))

$$\Pi(k) = \int_k^\infty T(p)\, dp. \tag{B.11}$$

Integrating (B.9), we obtain

$$\frac{d}{dt}\int_k^\infty E(p)\, dp + \int_k^\infty 2\nu p^2 E(p)\, dp = \int_k^\infty T(p)\, dp. \tag{B.12}$$

The rate of loss of energy by viscous dissipation is given by

$$\varepsilon(k) = \int_k^\infty 2\nu p^2 E(p)\, dp. \tag{B.13}$$

Thus,

$$\frac{d}{dt}\int_k^\infty E(p)\, dp = \Pi(k) - \varepsilon(k). \tag{B.14}$$

In a steady state the above equation implies that

$$\Pi(k) = \varepsilon(k). \tag{B.15}$$

An equation for the mean-squared concentration $\mathcal{C}(k)$ can be written as (McComb 1996):

$$\left(\frac{\partial}{\partial t} + 2Dk^2\right)\mathcal{C}(k) = T_c(k), \tag{B.16}$$

where $T_c(k)$ satisfies

$$\int_0^\infty T_c(k)\, dk = 0.$$

Like the energy nonlinearity, $T_c(k)$ conserves the mean-squared concentration. An analogous equation to (B.15) can be written for the concentration field as:

$$\Pi_c(k) = \varepsilon_c(k), \tag{B.17}$$

where $\Pi_c(k)$ is the total rate of concentration transfer from all wavenumbers lower than $k$ and to all wavenumbers higher than $k$ and $\varepsilon_c$ is the rate at which the mean-squared concentration is destroyed by molecular diffusivity.

## B.3 Kolmogorov's spectral picture

The usual interpretation of (B.9) (and similarly (B.16)) is that the energy in the system at small $k$ is transferred by the nonlinear term $T(k)$ to large $k$ where it is dissipated by the viscous term. The overall effect of the nonlinear term is the energy cascade. If we integrate (B.9) by setting the nonlinear term equal to zero and make the time dependence explicit we obtain

$$E(k,t) = E(k,t_0)\exp\left(-2\nu k^2 t\right).$$

It is clear that the decay of energy is faster for higher values of $k$. Kolmogorov noted that energy is dissipated primarily at high wavenumbers. In a range of intermediate wavenumbers, which he calls the inertial subrange, energy is cascaded downscale. The lower wavenumber limit of this range is determined by the size of the eddies that contain most of the turbulent kinetic energy (McComb 1996, and refs. therein).

On dimensional grounds, he introduced a characteristic length scale $(\nu^3/\varepsilon)^{1/4}$, which is now termed as the Kolmogorov microscale. The inverse of this is normally taken as the maximum possible wavenumber in the inertial transfer range, which we will denote by $k_v$, which is given by

$$k_v = \left(\frac{\varepsilon}{\nu^3}\right)^{1/4}.$$

One can verify that $E(k)$ has dimension $L^3T^{-2}$ and $\varepsilon$ has dimension $L^2T^{-3}$ (Leslie 1973). According to the Kolmogorov theory, $E(k)$ is independent of $\nu$ in the inertial subrange but does depend on $k$ and $\varepsilon$. It follows that the spectrum function $E(k)$ takes the form

$$E(k) \propto (\varepsilon)^{2/3} k^{-5/3}, \tag{B.18}$$

$$L^3T^{-2} \qquad \left(L^2T^{-3}\right)^{2/3} L^{5/3},$$

which is the famous Kolmogorov $k^{-5/3}$ law.

## B.4 Kolmogorov-type argument

It was postulated by Corrsin (1951) that the Kolmogorov hypothesis can be applied to the spectrum of mean-squared concentration. The general increase of gradients of $C$ caused by the irregular stirring action of the nonlinear term was realized to be a transfer between different Fourier components of the distribution of $C$. Unlike the upper limit of inertial range of energy transfer, it was proposed that the molecular

diffusion produces a cut-off in the concentration spectrum which is given by

$$k_c = \left(\frac{\varepsilon}{D^3}\right)^{\frac{1}{4}}.$$

Batchelor (1959) argued that the proposed diffusion cut-off $k_c$ is only valid for $S_c \ll 1$ and concluded that for $S_c \gg 1$ the cut-off would be

$$k_B = \left(\frac{\varepsilon}{\nu D^2}\right)^{\frac{1}{4}},$$

where we refer to $k_B^{-1}$ as the Batchelor microscale.

We begin with a systematic review of the dimensional analysis made by Obukhov (1949) and Corrsin (1951) based on the Kolmogorov hypothesis. Without going to their detailed arguments, we note that the expression

$$k_c = \left(\frac{\varepsilon}{D^3}\right)^{\frac{1}{4}}$$

is an obvious extension of the form for the Kolmogorov dissipation wavenumber, which is given by

$$k_v = \left(\frac{\varepsilon}{\nu^3}\right)^{\frac{1}{4}}.$$

We assume that the spectrum is a power law. For wavenumbers much smaller than either $k_c$ or $k_v$, simple dimensional analysis results in

$$\mathcal{C}(k) \sim \varepsilon_c \varepsilon^{-\frac{1}{3}} k^{-\frac{5}{3}}, \tag{B.19}$$

where $\varepsilon_c$ is the rate at which mean-squared concentration is destroyed by molecular diffusivity.

The Kolmogorov energy spectrum was modified by Bowman (1996), who suggested the modification

$$E(k) \;=\; \left(\frac{4}{3}\right)^{1/3} \bar{\varepsilon}^{2/3} k^{-5/3} \chi^{-1/3}(k) \quad (k \le k_0)\,, \tag{B.20}$$

where $\bar{\varepsilon}$ is proportional to the energy transfer rate $\varepsilon$ and $\chi(k)$ is a correction factor given by

$$\chi(k) \;=\; 1 - \frac{k_0^2}{k^2}\,(1 - \chi_0)\,, \tag{B.21}$$

where

$$\chi_0 \;=\; 4\bar{\varepsilon}^2 k_0^{-5} E^{-3}(k_0)/3 \;=\; \chi(k_0) > 0. \tag{B.22}$$

Kolmogorov suggested that the inertial energy transfer is a local phenomenon and that the transfer over a large wavenumber range is very small. We consider the fact that concentration is not created or destroyed within the inertial-range and interaction between eddies is the mechanism that redistributes it among the inertial-range of wavenumbers.

Due to the locality hypothesis of Kolmogorov, $\varepsilon_c$ should be proportional to the total concentration ($\sim k\mathcal{C}(k)$) in wavenumbers near $k$ and to some effective rate of shear $\eta$ which acts to distort the flow structures of scale $k^{-1}$. That is

$$\varepsilon_c \sim \eta k \mathcal{C}(k). \tag{B.23}$$

Following Kraichnan (1971) and Bowman (1996), the rate of shear $\eta$ is given by

$$\eta^2 \sim \int_0^k p^2 E(p) dp. \tag{B.24}$$

In the case of the energy spectrum we have, in analogy with (B.23),

$$\varepsilon \sim \eta k E(k). \tag{B.25}$$

Using (B.20) in (B.25), we obtain

$$\eta \sim \varepsilon^{1/3} k^{2/3} \chi^{1/3}(k). \tag{B.26}$$

Now (B.23) implies that

$$\mathcal{C}(k) \sim \frac{\varepsilon_c}{\eta k}.$$

Therefore, the concentration spectrum $\mathcal{C}(k)$ can be expressed in the following form

$$\mathcal{C}(k) \sim \varepsilon_c \varepsilon^{-1/3} k^{-5/3} \chi^{-1/3}(k). \tag{B.27}$$

However, in the case of the concentration spectrum, there are an infinite number of constants of motion and so taking a universal value of the proportionality coefficient in (B.19) is questionable (Kraichnan 1968).

It has been pointed out that the concentration spectrum becomes more complicated in the presence of an additional quantity, the Schmidt number (Batchelor 1959; Leslie 1973), which is defined by (B.1).

One can define two regimes:

- If $S_c \ll 1 \Rightarrow \nu \ll D$,
- If $S_c \gg 1 \Rightarrow \nu \gg D$.

So if we compare viscous cutoff with the diffusion cutoff, we get

$$k_c \ll k_v \text{ in case of } S_c \ll 1$$

and

$$k_c \gg k_v \text{ in case of } S_c \gg 1.$$

Either the Obukhov–Corrsin law (B.19) or the modified Obukhov–Corrsin law (B.27) is valid only for wavenumbers much smaller than either $k_c$ or $k_v$. We discuss below two wavenumber regimes, namely, $k_c \ll k \ll k_v$ and $k_v \ll k \ll k_c$.

**Case** $k_c \ll k \ll k_v$ : Batchelor pointed out that in the case of $D \gg \nu$, $k_c \ll k_v$ (Batchelor 1959; Leslie 1973). Hence the scalar spectrum will fall off much more rapidly than the energy spectrum for wavenumbers $p$ that are higher than $k_c$. Hence the convolution integral in (B.7) will be dominated by $p < k_c$. In the inertial range, where $\varepsilon$ and $\varepsilon_c$ are independent of $k$, it follows from (B.25) and (B.23) that

$$\mathcal{C}(k) \sim E(k).$$

Following Batchelor (1959) and McComb (1996), we can write down $\mathcal{C}(k)$ as below:

$$\mathcal{C}(k) \sim \varepsilon_c D^{-3} k^{-4} E(k). \tag{B.28}$$

Upon substituting the expression for $E(k)$ from (B.20) we get

$$\mathcal{C}(k) \sim \varepsilon_c \varepsilon^{2/3} D^{-3} k^{-17/3} \chi^{-1/3}(k), \tag{B.29}$$

where $\chi(k)$ is given by (B.21)

**Case $k_v \ll k \ll k_c$ Batchelor's model of turbulent fluid:** Here we describe the viscous-advection range based on Batchelor's model of turbulent fluid (Batchelor 1959). If we look at the spectrum of velocity gradients, which is $k^2 E(k)$, it can be noticed that (Leslie 1973)

$$k^2 E(k) \sim k^{1/3} \qquad \text{if} \quad k < k_v.$$

Since $E(k)$ falls off rapidly for wave numbers $k$ that are larger than $k_v$, the spectrum of velocity gradient also decreases in this region. Hence the spectrum of velocity gradient has a maximum near $k = k_v$. Batchelor assumes that $\dfrac{\partial u}{\partial x}$ will virtually be constant over regions of space of linear dimensions roughly $k_v^{-1} = (\nu^3/\varepsilon)^{1/4}$. These regions are called as 'blobs' of fluid. Because of the incompressibility constraint, each blob will have a constant volume. The changes of shape of blobs or straining motion causes the mean-squared concentration to be transfered to higher and higher wavenumbers.

Let the motion of the fluid in a blob be specified by

$$u = \alpha x, \quad v = \beta y, \quad w = \gamma z.$$

The incompressibility condition (2.15) leads to

$$\alpha + \beta + \gamma = 0. \tag{B.30}$$

If two of these parameters are positive then an initially spherical blob will be distorted into a flat disc. If two of these parameters are negative, this initially spherical blob will be distorted into a needle shape.

Let $\gamma$ be the most negative rate of strain parameter and $z$ be the direction of least principal rate of stain. Following Batchelor (1959) and Leslie (1973), one can write down

$$|\gamma| \sim n_1(\varepsilon/\nu)^{1/2}. \tag{B.31}$$

Batchelor infers from experimental evidence that

$$n_1 \quad \sim \quad 0.05.$$

Thus, if the blob is strained in one direction, say the $z$ direction, the variations of $C$ will be concentrated only in that direction. In such a situation one may approximate the non-linear term by the Fourier transform of (B.16) (Leslie 1973)

$$|\gamma| z \frac{d}{dz}\langle CC\rangle \tag{B.32}$$

Inserting this approximation into (B.16) we obtain

$$\begin{aligned} T_c(k) &= |\gamma| \left( i^2 k \frac{\partial \mathcal{C}(k)}{\partial k} - \mathcal{C}(k) \right) \\ &= -|\gamma| \frac{\partial}{\partial k} \left( k\mathcal{C}(k) \right). \end{aligned}$$

A stationary solution of (B.16) would then require that

$$\begin{aligned} 2Dk^2\mathcal{C}(k) &= -|\gamma|\frac{\partial}{\partial k}\left(k\mathcal{C}(k)\right), \\ -\frac{2Dk}{|\gamma|}dk &= \frac{d(k\mathcal{C}(k))}{k\mathcal{C}(k)}, \\ -\frac{Dk^2}{\gamma} &= \ln(k\mathcal{C}(k)) + \text{const}, \\ \mathcal{C}(k) &\sim k^{-1}\exp\left(-\frac{Dk^2}{|\gamma|}\right). \end{aligned}$$

So that

$$\mathcal{C}(k) \sim k^{-1}\exp\left(-\frac{Dk^2}{n_1(\frac{\varepsilon}{\nu})^{1/2}}\right). \tag{B.33}$$

If we look at the exponential term, we see that

$$-\frac{Dk^2}{n_1(\frac{\varepsilon}{\nu})^{1/2}} = -\frac{1}{n_1}\left(\frac{k_v}{k_c}\right)^{4/3}\left(\frac{k}{k_v}\right)^2 \ll 1.$$

Thus we can write the spectrum function in the following form

$$\mathcal{C}(k) \sim k^{-1}. \tag{B.34}$$

This is the Batchelor formula for the mean-squared concentration. Thus if $S_c \gg 1$, which is the case for most of the fluid, the mean-squared concentration satisfies the Batchelor spectrum for wave numbers higher than $k_v$ but lower than $k_c$.

In this discussion, we have obtained the correction (B.27) to the Obukhov-Corrsin law (B.19). This correction is similar to that proposed by Bowman (1996) for the three-dimensional energy inertial range.

# Bibliography


[Allison & Nambi 1994] S. A. Allison & P. Nambi, Macromolecules, **27**:1413, 1994.

[Ames 1977] W. F. Ames, *Numerical Methods for Partial Differential Equations*, Academic Press, San Diego, California, 1977.

[Andreev & Lisin 1993] V. P. Andreev & E. E. Lisin, Chromatograhia, **37**:202, 1993.

[Arulanandam & Li 2000] S. Arulanandam & D. Q. Li, Journal of Colloid and Interface Science, **225**:421, 2000.

[Batchelor 1959] G. Batchelor, J.Fluid.Mech., **49**:113, 1959.

[Bier 1959] M. Bier, *Electrophoresis:Theory, methods and applications*, Academic Press, San Diego, California, 1959.

[Boris & Book 1964] J. Boris & D. Book, Journal of Computational Physics, **11**:38, 1964.

[Boris & Book 1976] J. Boris & D. Book, Methods in Computational Physics, **16**:85, 1976.

[Bowen *et al.* 1976] B. D. Bowen, S. Levine, & N. Epstein, Journal of Colloid and Interface Science, **54**:375, 1976.

[Bowman *et al.* 2000] J. C. Bowman, A. Zeiler, & D. Biskamp, Journal of Computational Physics, **158**:239, 2000.

[Bowman 1996] J. C. Bowman, J.Fluid.Mech., 1996.

[Briggs 1987] W. I. Briggs, *A multigrid tutorial*, SIAM, Pennsylvania, 1987.

[Burgreen & Nakache 1964] D. Burgreen & F. R. Nakache, J. Phys. Chem.., **68**:1084, 1964.

[Corrsin 1951] S. Corrsin, Journal Applied Physics, **22**:469, 1951.

[Courant *et al.* 1952] R. Courant, E. Isaacson, & M. Rees, Comm. Pure Appl. Math., **5**:243, 1952.

[Crabtree *et al.* 2000] H. J. Crabtree, E. C. Cheong, D. A. Tilroe, & C. J. Backhouse, Microchip injection and separation anomalies due to siphoning., Unpublished., 2000.

[Culbertson & Jorgenson 1994] C. T. Culbertson & J. W. Jorgenson, Anal. Chem., **66**:955, 1994.

[Ermakov *et al.* 1998] S. V. Ermakov, S. C. Jacobson, & J. M. Ramsey, Anal. Chem., **70**:4494, 1998.

[Ermakov *et al.* 2000] S. V. Ermakov, S. C. Jacobson, & J. M. Ramsey, Anal. Chem., **15**:3512, 2000.

[Gaál *et al.* 1980] O. Gaál, G. A. Medgyesi, & L. Vereczkey, *Electrophoresis in the Separation of Biological Macromolecules*, John Wiley & Sons, New York, 1980.

[Hackbusch 1985] W. Hackbusch, *Multigrid methods and applications*, Springer-Verlag, New York, 1985.

[Harrison *et al.* 1992] D. J. Harrison, A. M. Z., F. H. Ludi, & H. M. Widmer, Anal. Chem., **64**:1926, 1992.

[Harrison *et al.* 1993] D. J. Harrison, P. G. Glavina, & A. Manz, Sens. Actuators, **10**:107, 1993.

[Holt 1984] M. Holt, *Numerical Methods in Fluid Dynamics*, Springer-Verlag, New York, 1984.

[Jia 1998] W. Jia, Transactions of the Japan Society for Aeronautical and Space Sciences, **41**:105, 1998.

[Jorgenson & Lukacs 1981] J. W. Jorgenson & K. D. Lukacs, Anal. Chem., **53**:1292, 1981.

[Kolmogorov 1941] A. N. Kolmogorov, C. R. Acad. Sci. U.S.S.R., **30**:301, 1941.

[Kraichnan 1968] R. H. Kraichnan, The Physics of Fluid, **11**:945, 1968.

[Kraichnan 1971] R. H. Kraichnan, J. Fluid. Mech., **47**:525, 1971.

[Kundu 1990] P. K. Kundu, *Fluid Mechanics*, Academic Press, San Diego, California, 1990.

[Leslie 1973] D. Leslie, *Developments in the theory of turbulence*, Clarendon Press, Oxford, 1973.

[LeVeque 1990] R. J. LeVeque, *Numerical Methods for Conservation Laws*, Birkhauser Verlag, Boston, 1990.

[Levine & Neale 1976] S. Levine & G. H. Neale, Journal of Colloid and Interface Science, **47**:520, 1976.

[McComb 1996] W. D. McComb, *The Physics of Fluid Turbulence*, Clarendon Press, Oxford, 1996.

[Minev & Ethier 1999] P. D. Minev & C. R. Ethier, Journal, **5**, 1999.

[Morrison & Stukel 1970] F. A. Morrison, JR. & J. J. Stukel, Journal of Colloid and Interface Science, **33**:88, 1970.

[Moyer & Gorin 1990] H. A. A. L. S. Moyer & M. H. Gorin, *Electrophoresis of proteins and the chemistry of cell surfaces*, Academic Press, San Diego, California, 1990.

[Neumann & Richtmyer 1950] J. V. Neumann & R. D. Richtmyer, J. Appl. Phys., **21**:232, 1950.

[Obukhov 1949] A. M. Obukhov, Izv. Akad. Nauk, **13**:58, 1949.

[Patankar & Hu 1998] N. A. Patankar & H. H. Hu, Anal. Chem, **70**:1870, 1998.

[Press *et al.* 1997] W. H. Press, S. A. Teukolsky, W. T. Vetterling, & B. P. Flannery, *Numerical Recipes in C: The art of scientific computing*, Cambridge University Press, Cambridge, 1997.

[Reed & Morrison 1976] L. D. Reed & F. A. Morrison, Jr., Journal of Colloid and Interface Science, **54**:117, 1976.

[Rice & Whitehead 1965] C. Rice & R. Whitehead, The Journal of Physical Chemistry, **69**:4017, 1965.

[Richtmyer & Morton 1957] R. D. Richtmyer & K. W. Morton, *Difference Methods for Initial-Value Problems*, Interscience Publishers, New York, 1957.

[Ritchie 1986] H. Ritchie, American Meteorological Society, **114**:135, 1986.

[Roache 1972] P. J. Roache, *Computational fluid dynamics*, Hermosa publishers, Albuquerque, 1972.

[Schlichting 1968] H. Schlichting, *Boundary-Layer Theory*, McGraw-Hill Book Company, New York, 1968.

[Schulz 1964] W. D. Schulz, Methods in Computational Physics, **3**:1, 1964.

[Seiler *et al.* 1994] K. Seiler, H. Z. Fan, K. Fluri, & D. J. Harrison, Anal. Chem, **66**:3485, 1994.

[Sidilkover & Ascher 1995] D. Sidilkover & U. M. Ascher, Computational and Applied Mathematics, **14**:21, 1995.

[Skoog *et al.* 1998] D. A. Skoog, F. J. Holler, & T. A. Nieman, *Principles of Instrumental Analysis*, Sanunders College Publishing, Chicago, 1998.

[Staniforth & Cote 1991] A. Staniforth & J. Cote, American Mathematical Society, **119**:2206, 1991.

[Stuart 1961] R. Stuart, *An introduction to Fourier analysis*, John Wiley and Sons Inc, New York, 1961.

[Tannehill *et al.* 1997] J. C. Tannehill, D. A. Anderson, & R. H. Pletcher, *Computational Fluid Mechanics and Heat transfer*, Taylor and Francis, 1997.

[Woodward & Colella 1984] P. Woodward & P. Colella, Journal of Computational Physics, **54**:115, 1984.